



HAL
open science

Deformation, crustal melting and magmatism in the crustal-scale East-Variscan Shear Zone (Aiguilles-Rouges and Mont-Blanc massifs, Western Alps)

Jonas Vanardois, Pierre Trap, Françoise Roger, Jérémie Melleton, Didier Marquer, Jean-Louis Paquette, Philippe Goncalves, Florence Cagnard, Benjamin Le Bayon

► To cite this version:

Jonas Vanardois, Pierre Trap, Françoise Roger, Jérémie Melleton, Didier Marquer, et al.. Deformation, crustal melting and magmatism in the crustal-scale East-Variscan Shear Zone (Aiguilles-Rouges and Mont-Blanc massifs, Western Alps). *Journal of Structural Geology*, 2022, 163, pp.104724. 10.1016/j.jsg.2022.104724 . hal-03790246

HAL Id: hal-03790246

<https://brgm.hal.science/hal-03790246>

Submitted on 26 Oct 2022

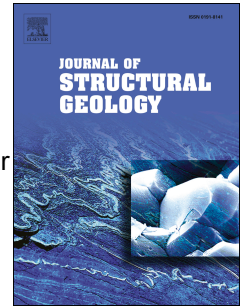
HAL is a multi-disciplinary open access archive for the deposit and dissemination of scientific research documents, whether they are published or not. The documents may come from teaching and research institutions in France or abroad, or from public or private research centers.

L'archive ouverte pluridisciplinaire **HAL**, est destinée au dépôt et à la diffusion de documents scientifiques de niveau recherche, publiés ou non, émanant des établissements d'enseignement et de recherche français ou étrangers, des laboratoires publics ou privés.

Journal Pre-proof

Deformation, crustal melting and magmatism in the crustal-scale East-Variscan Shear Zone (Aiguilles-Rouges and Mont-Blanc massifs, Western Alps).

Jonas Vanardois, Pierre Trap, Françoise Roger, Jérémie Melleton, Didier Marquer, Jean-Louis Paquette, Philippe Goncalves, Florence Cagnard, Benjamin Le Bayon



PII: S0191-8141(22)00216-4

DOI: <https://doi.org/10.1016/j.jsg.2022.104724>

Reference: SG 104724

To appear in: *Journal of Structural Geology*

Received Date: 17 March 2022

Revised Date: 2 September 2022

Accepted Date: 9 September 2022

Please cite this article as: Vanardois, J., Trap, P., Roger, Franç., Melleton, Jéré., Marquer, D., Paquette, J.-L., Goncalves, P., Cagnard, F., Le Bayon, B., Deformation, crustal melting and magmatism in the crustal-scale East-Variscan Shear Zone (Aiguilles-Rouges and Mont-Blanc massifs, Western Alps)., *Journal of Structural Geology* (2022), doi: <https://doi.org/10.1016/j.jsg.2022.104724>.

This is a PDF file of an article that has undergone enhancements after acceptance, such as the addition of a cover page and metadata, and formatting for readability, but it is not yet the definitive version of record. This version will undergo additional copyediting, typesetting and review before it is published in its final form, but we are providing this version to give early visibility of the article. Please note that, during the production process, errors may be discovered which could affect the content, and all legal disclaimers that apply to the journal pertain.

© 2022 Published by Elsevier Ltd.

1 **Deformation, crustal melting and magmatism in the crustal-scale East-Variscan Shear Zone**
2 **(Aiguilles-Rouges and Mont-Blanc massifs, Western Alps).**

3

4 Jonas Vanardois^{1*}, Pierre Trap², Françoise Roger³, Jérémie Melleton⁴, Didier Marquer², Jean-
5 Louis Paquette⁵, Philippe Goncalves², Florence Cagnard⁴ and Benjamin Le Bayon⁴

6 vanar030@umn.edu; pierre.trap@univ-fcomte.fr; francoise.roger@umontpellier.fr;

7 j.melleton@brgm.fr ; didier.marquer@univ-fcomte.fr; j.l.paquette@opgc.univ-

8 bpclermont.fr; philippe.goncalves@univ-fcomte.fr; f.cagnard@brgm.fr; b.lebayon@brgm.fr

9 ¹Department of Earth Sciences, University of Minnesota, Minneapolis, MN 55455, USA

10 ²UMR 6249 Chrono-environnement, Université de Bourgogne-Franche-Comté, 25030
11 Besançon, France.

12 ³Géosciences Montpellier, Campus Triolet, Université Montpellier, CNRS, 34095 Montpellier
13 Cedex 5, France.

14 ⁴BRGM-French Geological Survey, 3 Avenue Claude Guillemin, 45100, Orléans, France.

15 ⁵Laboratoire Magmas et Volcans (CNRS-UMR 6524), Campus Universitaire des Cézeaux, 63178
16 Aubière Cedex, France.

17

18 *Corresponding author: vanar030@umn.edu; +33606755562; Present address: 116 Church
19 Street SE, John H. Tate Hall suite 150, Minneapolis, MN 55455.

20

21 **Key points:** Variscan Belt, Transpression, Structural analysis, Zircon and monazite LA-ICMPS
22 U-Th-Pb dating, crustal-scale East Variscan Shear Zone

23

24 **Abstract**

25 The Aiguilles-Rouges and Mont-Blanc massif represent a segment of a crustal-scale
26 transpressional shear zone named the East Variscan Shear Zone (EVSZ) along which two
27 plutonic pulses occurred during Early and Late Carboniferous times. The aim of this study is to
28 constrain the relationships between the dynamics of the crustal-scale shear zone, the
29 mechanisms of pluton emplacement at different structural levels within the crust and the
30 magma sources. A detailed structural analysis of the whole massif highlights the crustal-scale
31 anastomosed network of the EVSZ. Microstructural observations and LA-ICPMS U-Th-Pb zircon
32 ages from large plutons constrain the beginning of the transpression at ca. 340 Ma. From 340
33 to 305 Ma, the EVSZ broadened and formed a 25 km-wide dextral S-C-C' anastomosed shear
34 zone network with dilation zones acting as preferential pathways for melt migration and
35 pluton growths. Moreover, LA-ICPMS U-Th-Pb zircon ages from small magmatic bodies (i.e.
36 pegmatite, aplite and microgranite) indicate an Ordovician-age inheritance component. Field
37 evidences and zircon inheritance indicate that Late Carboniferous granitic melts are mainly
38 derived from water-fluxed melting of Ordovician orthogneiss with the input of mantellic-
39 source derived magmas. Over time, the growth of the dextral anastomosed network enhanced
40 water transfer through the shear zones and water-fluxed melting to produce more anatectic
41 melts.

42

43 **1. Introduction**

44 Continent-scale shear zones are pathways along which ductile and brittle deformation leads
45 to segregation and transport of melts from deep to shallow crustal levels where syn-kinematic
46 plutons might be emplaced (e.g. D'Lemos et al., 1992; Tikoff and Teyssier, 1994; Tommasi et
47 al., 1994; Brown and Solar, 1998; Brown, 2013). Large crustal-scale shearing may last tens of
48 millions of years (Oriolo et al., 2018; Carosi et al., 2022) but may also be the sum of localized
49 and transient events (e.g. Fossen and Cavalcante, 2017). The duration and amount of melt
50 production depends on main parameters such as the rock composition, melting reactions,
51 mantle and crustal heat flux and the amount of water. Recently, water-fluxed crustal melting
52 has been increasingly regarded as an important mechanism for initiation of voluminous
53 melting (Weinberg and Hasalová, 2015) and for production of large batholiths (Collins et al.,
54 2016) as an alternative to biotite or amphibole dehydration melting. This issue of the
55 contribution of water-fluxed melting is disputed (Clemens and Stevens, 2015) and remains to
56 be tackle.

57 The dynamics of granitic pluton emplacement depends on the source of melts and the
58 geodynamic context (e.g. Jacob et al., 2022). The timing of pluton emplacement depends on
59 their volume and progressive infilling rates, and large batholiths ($>10 \text{ km}^3$) can grow at rates
60 of about 1-10 Ma (Brown, 2013; de Saint Blanquat et al., 2011). Pluton emplacements in large-
61 scale shear zones can induce local stress field and modify the regional strain partitioning (e.g.
62 Brun and Pons, 1981; Neves et al., 1996). To fully understand the genesis and emplacement
63 of granitic magmas along crustal-scale shear zones, timing, rates and interplay between

64 processes like shear deformation, melt production, melt and aqueous fluid transfer, pluton
65 growth and emplacement must be further examined.

66 In the Western Alps, the Aiguilles-Rouges (AR) and Mont-Blanc (MB) massifs expose sections
67 of middle and upper crust where migmatites and syn-kinematic Carboniferous granitic plutons
68 are spatially and temporally correlated with the continental-scale East-Variscan Shear Zone
69 (EVSZ; Guillot et al., 2009; Simonetti et al., 2020) (Fig. 1A). Previous geochronological studies
70 have documented two distinct magmatic events at ca. 340-330 Ma and ca. 310-300 Ma (von
71 Raumer and Bussy, 2004 and references therein). This twofold Carboniferous plutonism is
72 typical for the Variscan basement of the External Crystalline Massifs (ECMs) of the Alps (Debon
73 and Lemmet, 1999) and other parts of the Variscan belt (Corsica-Sardinia: Paquette et al.,
74 2003; Rossi et al., 2009; Vosges: Tabaud et al., 2014, 2015). In the AR and MB massifs, the
75 Early Carboniferous plutons are small (ca. 1-2 km²) and emplaced in the upper crust whereas
76 the Late Carboniferous plutons are large, with an approximate area of ca. 20 to 200 km² (Bussy
77 et al., 2000). These large plutons growth and crystallized in the migmatitic middle crust. The
78 source of the granitic melts is thought coming from the deep part of the over thickened
79 continental crust (Bussy, 1990; von Raumer and Bussy, 2004). Synchronous basic intrusions
80 and peraluminous dykes (Bussy et al., 2000) suggest that the source is more complex. Also,
81 the draining structures and melt-present deformation history can be better understood.

82 We present a multi-scale structural analysis performed to define the strain pattern of the EVSZ
83 and the relationships with syn-kinematic granitic intrusions in the AR and MB massifs. Field
84 work and LA-ICPMS U-Th-Pb zircon and monazite ages provide new insights about the nature
85 of the protolith source, partial melting and emplacement age of magmatic bodies within the
86 metamorphic basement. We propose a model for the production, ascent and emplacement

87 of granitic magmas within the EVSZ. It emphasizes the importance of water-fluxed crustal
88 melting and the occurrence of kilometre-scale dilation zones controlling melt transfers from
89 the anatectic source to the pluton sink.

90

91 **2. Geological setting**

92 The AR and MB massifs, located in the western Alpine external domain, are two narrow NE-
93 SW trending Variscan massifs bounded by autochthonous and allochthonous Mesozoic
94 sedimentary rocks (Fig. 1B). These two massifs, part of the ECMs, represent an exhumed
95 portion of the Variscan crust deformed between ca. 340 and 300 Ma (e.g. von Raumer and
96 Bussy, 2004; Vanardois et al., 2022) (Fig. 1). Structures in the AR massif suggests dextral
97 transpression (von Raumer and Bussy, 2004) and the Emosson-Bérard Shear Zone (EBSZ) is
98 interpreted as a branch of the EVSZ network (Simonetti et al., 2020). However, the meter to
99 regional scale strain pattern of the whole AR and MB massifs has not been documented yet.
100 Besides, the place of the EVSZ and ECMs within the Variscan belt reconstruction are debated
101 (see Fig. 1A for instance) (e.g. Ballèvre et al., 2018; Simonetti et al., 2020; Martinez-Catalan et
102 al., 2021; Faure and Ferrière, 2022).

103 The AR and MB massifs are composed of Proterozoic and Cambro-Ordovician amphibolitic
104 facies gneissic basement and two greenschists facies or unmetamorphosed Carboniferous
105 basins (Servoz and Salvan-Dorénaz synclines respectively) (Fig. 1B). The protolith of the
106 gneissic basement consists of an upper Proterozoic to Cambrian sedimentary and
107 volcanoclastic sequence intruded by Ordovician granite laccoliths (Bussy et al., 2011; Paquette
108 et al., 1989; Fig. 1B). Two metamorphic events are distinguished. The first, related to collision

109 and crustal thickening, consists of a mid- to high-pressure metamorphism recorded as garnet-
110 kyanite bearing assemblage in micaschists and paragneisses, and as omphacite-bearing
111 eclogitic assemblage within tholeiitic metamafic lenses (von Raumer and Schwander, 1985;
112 von Raumer and Bussy, 2004; Liégeois and Duchesne, 1981; Vanardois et al., 2022). High-
113 pressure conditions have been estimated at 1.6-1.85 GPa and 680-750°C for the Lac Cornu
114 eclogites (Vanardois et al., 2022), and 1.3-1.5 GPa and 650-750°C for the Val Bérard eclogites
115 (Schulz and von Raumer, 1993, 2011) (see Fig. 1B for locations). Recently, LA-ICPMS U-Th-Pb
116 analyses on zircon and rutile from a Lac Cornu eclogite specimen has dated the HP
117 metamorphism at 340-330 Ma and the emplacement age of the protolith at ca. 460 Ma
118 (Vanardois et al., 2022). The AR and MB massifs were subsequently metamorphosed at
119 pressures between 0.2 and 0.6 GPa and temperatures at ~600-750°C (Dobmeier, 1996, 1998;
120 Schulz and von Raumer, 1993, 2011; von Raumer et al., 1996; Chiaradia, 2003; Marshall et al.,
121 1997; Genier et al., 2008).

122 The development of the main fabric in the AR massif is coeval with the HT-LP metamorphism.
123 It consists of sub-vertical 330 to 030 striking foliations bearing a sub-horizontal mineral
124 lineation. Dextral kinematic indicators are common (Bellière, 1958; von Raumer and Bussy,
125 2004; Simonetti et al., 2020) within centimeter- to meter-sized mylonites, documented in the
126 whole gneissic basement (von Raumer and Bussy, 2004). Moreover, a hectometer-sized
127 mylonitic zone is described near the Lac Emosson (Joye, 1989; Genier et al., 2008; Simonetti
128 et al., 2020). This shear zone recorded dextral transpression (von Raumer and Bussy, 2004;
129 Joye, 1989; Simonetti et al., 2020). Bellière (1958) proposed a crustal-scale structural model
130 but modern concepts like strain partitioning, heterogeneous or supra/subsolidus deformation
131 fabrics are not considered or documented at the scale of the whole AR and MB massifs. Relics

132 of earlier planar fabrics are reported in several studies (Bellière, 1958; Joye, 1989; von
133 Raumer, 1984; von Raumer and Bussy, 2004). In the Lac Cornu area (see Fig. 1B for location),
134 Vanardois et al. (2022) interpreted an early sub-horizontal foliation as the result of horizontal
135 flow of the partially molten crust.

136 Partial melting in the AR and MB massifs started during the HT-HP metamorphism, at near
137 peak pressure conditions at ~ 1.3 - 1.85 GPa at ca. 340-330 Ma (Vanardois et al., 2022). Ongoing
138 partial melting occurred during decompression and subsequent HT-LP metamorphism (Genier
139 et al., 2008). The metamorphic peak recorded in metapelitic rocks from the Emosson area (see
140 Fig. 1B for location) and the crystallization age of the anatectic melts occurred at 327 ± 2 Ma
141 and 320 ± 1 Ma, respectively (ID-TIMS U-Pb on monazite, Bussy et al., 2000). Cordierite-
142 bearing migmatites in the Fully area (Krummenacher, 1959) (see Fig. 1B for location) yield ID-
143 TIMS zircon ages at ca. 307 Ma (Bussy et al., 2000). In the MB massif, Bussy and von Raumer
144 (1994) dated leucogranitic injections into dextral shear bands at 317 ± 2 Ma (ID-TIMS U-Pb on
145 monazite). It remains unclear if the gneissic basement underwent one protracted partial
146 melting event lasting from ca. 330 to 307 Ma or two distinct episodes at ca. 330-315 Ma and
147 ca. 307 Ma.

148 In the Servoz area (see Fig. 1B), a Visean sequence is composed of metagreywackes, phyllites
149 and metavolcano-sedimentary rocks overlying fine-grained gneisses ("Pormenaz gneisses" in
150 Fig. 1B) (Dobmeier et al., 1999). It is affected by the transcurrent shearing under greenschist
151 to low amphibolite facies metamorphism (Dobmeier, 1996, 1998; Bellière and Streeel, 1980).
152 The uppermost Variscan crust is composed of Late Carboniferous fluvial and volcanic rocks
153 (Pilloud, 1991; Capuzzo and Wetzel, 2004) lying (1) in the upper part of the Servoz syncline
154 and (2) in the Salvan-Dorenaz syncline that are unconformably deposited over the Variscan

155 metamorphic rocks (Dobmeier and von Raumer, 1995; Lox and Bellière, 1993) (Fig.1B). These
156 rocks were metamorphized by the Alpine deformation at temperatures lower than 350 °C
157 (Boutoux et al., 2016). Dobmeier and von Raumer (1995) considered that these rocks were
158 not affected by Variscan deformation, whereas Lox and Bellière described Variscan open folds
159 with subvertical axial planes oriented N020 but without more details about any tectonic
160 significance.

161 The syn-kinematic Vallorcine granite emplaced along the EBSZ at 306.5 ± 1.5 Ma during dextral
162 transpression (ID-TIMS U-Pb on zircon and monazite; Bussy et al., 2000). Similar emplacement
163 ages (ID-TIMS U-Pb on zircon) at $307 +6/-5$ Ma, 303 ± 2 Ma and 304 ± 3 Ma are reported for
164 the Montenvers and the Mont-Blanc granites (Bussy and von Raumer, 1993, 1994) (Fig. 1B).
165 The Mont-Blanc and Montenvers granites are cross-cut by local subsolidus mylonites (Bussy,
166 1990; Bussy et al., 2000). The Morcles microgranite is meter-sized dykes dated at 303 ± 3 Ma,
167 304 ± 1 Ma and 311 ± 2 Ma (LA-ICPMS U-Th-Pb on zircon) and are interpreted as a shallow
168 extension of the Vallorcine granite (Bussien et al., 2017) (Fig.1B). Rhyolitic dykes of the MB
169 massif and dacites in the Salvan-Dorenaz syncline have been dated at 307 ± 2 Ma and 308 ± 3
170 Ma, respectively (ID-TIMS U-Pb on zircon; Capuzzo and Bussy, 2000) (Fig. 1B). The Visean rocks
171 of the Servoz syncline are intruded by the peraluminous Montées-Pélissier monzogranite and
172 the metaluminous Pormenaz monzonite, dated at 331 ± 2 Ma and 332 ± 2 Ma, respectively
173 (ID-TIMS U-Pb on zircon; Bussy et al., 2000) (Fig. 1B). These two granites, represent a first
174 magmatic pulse at ca. 330 Ma. Several authors propose that the Pormenaz and Montées-
175 Pélissier plutons are syn-tectonic granites emplaced along vertical shear zones during bulk
176 dextral shearing (Bussy et al., 2000; Dobmeier, 1996, 1998).

177 In the basement, Alpine tectonics and metamorphism are limited to the development of shear
178 zones active under greenschist facies conditions (Rolland et al., 2003; Rossi et al., 2005). In the
179 surrounding Mesozoic sedimentary cover, Alpine metamorphism did not exceed 350°C
180 (Boutoux et al., 2016). Alpine tectonics is also responsible for the pinch of the NE-SW
181 elongated Carboniferous Salvan-Dorenaz syncline (Fig. 1B) (Pilloud, 1991). Variscan tectono-
182 metamorphic imprint is widespread in the AR and MB with higher-grade metamorphic
183 conditions easily distinguishable from the lower-grade rocks in the Alpine localized shear
184 zones (e.g. von Raumer and Bussy, 2004; Simonetti et al., 2020).

185

186 **3. Structural data**

187 *3.1. D1 deformation*

188 D1 deformation is recorded in the gneissic basement by a sub-horizontal S1 foliation that dips
189 gently to the NE with an L1 O20-trending mineral lineation plunging at about 15° (Fig. 2B).
190 Although S1 fabric has been transposed by subsequent D2 deformation, it is locally preserved
191 at the outcrop-scale and at the regional-scale in the Pormenaz and Arpille areas (Fig. 2 and 3).
192 In domains where D2 deformation is pervasive, S1 foliation is transposed and folded into open
193 to isoclinal upright folds (Fig. 3 and 4A to D) or remains recognizable only in the hinge zones
194 of F2 folds. Few rootless isoclinal folds (F1) have been recognized in the preserved D1 domains
195 where an older planar fabric, designated Sx, is only locally observed in the hinges of F1 folds.
196 (Fig. 4D and F). In the preserved domains, kinematic indicators such as asymmetrical
197 boudinage, mica-fish and S-C fabrics indicate top-to-the-E and NE kinematics (Fig. 4E to H).

198 In the Lac Cornu area (see Fig. 1 and 2 for locations), the D1 deformation is defined by an S1
199 compositional layering in stromatitic orthogneiss migmatites (Fig. 4C), and within the core of
200 boudins of retrogressed eclogite (Vanardois et al., 2022). In the Arpille massif (Fig. 1B), S1
201 foliation is defined by the shape and preferential alignment of the leucosomes in anatectic
202 metapelites and metagraywackes (Fig. 4A). In the Pormenaz area, the S1 and L1 fabrics are
203 observed in the non-anatectic fine-grained Pormenaz gneiss (Fig. 4H).

204 3.2. D2 deformation

205 3.2.1. D2 deformation at the outcrop scale

206 D2 main fabric in the migmatitic basement and in the greenschist facies rocks of the Servoz
207 syncline is an S2 sub-vertical foliation striking 150-170 (Fig. 2C). In D1 preserved domains, S2
208 is a weak crenulation cleavage that strikes \sim N160 (Fig. 4A to D). A decameter-wide strain
209 gradient from the D1 preserved domains toward the S2 pervasive foliation is observed with
210 the progressive tightening of F2 folds and the reorientation of the S1 sub-horizontal foliation
211 into a sub-vertical position. Steeply-dipping and 160-striking axial planes of F2 folds are sub-
212 parallel to S2 foliation. F2 fold axes plunge shallowly to steeply along the 160-striking axial
213 planes. In pervasive D2 domains, we observed S-C-C' fabrics where vertical C2 shear bands
214 striking 000-020 progressively reorient S2 foliations and become the main planar fabric,
215 before being reoriented by the vertical C'2 shear bands striking 020-040 (Fig. 5A to C).

216 In the Lac Cornu migmatites, the S2 foliation is defined by mineralogical layering in the
217 stromatic migmatite. Injections of melt in the C2 and C'2 shear bands (Fig. 5A) argue for
218 suprasolidus conditions of shearing in this part of the massif. In the Lac Cornu metamafic
219 lenses, the retrogression of the eclogite facies to amphibolitic facies is associated with D2

220 (Vanardois et al., 2022). In the Fully area (see Fig. 1 for location), cordierite-bearing migmatites
221 show a gneissic layering and cordierite clots sub-parallel to the orientation of $C'2$ shear bands.
222 Migmatites are also affected by centimeter-sized ultramylonitic bands sub-parallel to $C'2$
223 fabric (Fig. 5D). $S2$, $C2$ and $C'2$ planar fabrics are commonly associated with a shallowly N-
224 plunging (30°) $L2$ mineral lineation (Fig. 2C). The $D2$ deformation is conspicuously associated
225 with dextral kinematics highlighted by shear criteria and the $S-C-C'$ fabrics (Fig. 5).

226 3.2.2. $D2$ architecture at the regional scale

227 The compilation of all measurements of planar fabrics related to $D2$ led to a well-defined
228 three-fold subdivision: a first group labelled as $S2$ (150-170), a second group labelled as $C2$
229 (000-020) and a third group labelled as $C'2$ (020-040) (Fig. 2C). Where one of the three planar
230 fabrics ($S2$, $C2$ or $C'2$) is predominant at the outcrop scale, the corresponding orientation is
231 considered to build the foliations trajectory map of figure 2. One may notice that $S2$ foliation
232 is predominant in the western and upper structural levels (Servoz-Pormenaz-Brevent areas)
233 whereas the eastern AR massif shows mostly $C2$ and $C'2$ planar fabrics (Fig. 2). The $S-C-C'$
234 regional structure resemble the one observed at all scales from millimetre to decametre.
235 Furthermore, pervasive $C2$ and $C'2$ -domains form three main kilometre-wide dextral shear
236 zones: the Cornu Shear Zone (CSZ), the Montenvers (MSZ) and Emosson-Bérard shear zones
237 (EBSZ). The orientation of these structures is in good agreement with a massif-scale $S-C-C'$ -like
238 structures.

239 3.3. $D3$ deformation

240 $D3$ structures are only observed in the south-western part of the AR massif, within the
241 Pormenaz gneiss and the Viséan metasedimentary rocks (Fig. 2, 6 and 7). $D3$ is recorded in

242 metre- to decametre-sized domains where D2 deformation is folded by open to tight F3 folds
243 with a sub-horizontal S3 cleavage (Fig. 6, 7 and 8). S3 cleavage and F3 fold axial planes are sub-
244 parallel, and are both gently E-dipping (Fig. 6B). F3 folds axes are gently SE-plunging. L3
245 lineation has been only locally observed (Fig. 6B) and corresponds to an intersection lineation
246 between S2 and S3 fabrics. Due to the lack of mineral or stretching L3 lineation, kinematics of
247 D3 deformation remains unknown. D3 fabrics are defined by typical greenschist facies
248 minerals such as chlorite (Fig. 8B). Few quartz-feldspar bearing leucocratic bodies interpreted
249 as leucosomes are folded by the S3 fabric (Fig. 8C).

250

251 **4. Description of dated samples**

252 Eleven samples of magmatic rocks have been sampled from different locations of the
253 “plumbing” in the AR and MB massifs, corresponding to five large magmatic bodies: Couteray
254 orthogneiss (AR37), Pormenaz granite (AR801), Montées-Pélissier granite (AR865), Vallorcine
255 granite (AR73), Montenvers granite (MB43), Mont-Blanc granite (MB37); and four smaller
256 bodies: Morcles microgranite (AR1028) and pegmatitic and aplitic dykes (AR833, AR1020,
257 AR1006 and AR916). See Figs. 1, 3, and 7, and Table 1 for sample locations. Mineral
258 assemblages are detailed in Table 1..

259 *4.1. Large magmatic bodies*

260 The Couteray orthogneiss (AR37) is a N-S-trending elongate meta-igneous body located in the
261 Val Bérard near the Vallorcine granite (Fig. 1B and 3A). It shows well-pronounced N-S D2
262 deformation, corresponding to C2 and C'2 planes based on their orientations, clearly

263 indicative of dextral shearing (Fig. 9A). Local myrmeckite are observed in shear bands passing
264 through large K-feldspar grains (Fig. 9A).

265 The Pormenaz granite (AR801) emplaced in the gneisses of the eastern limb of the Servoz
266 syncline (Fig. 1B). Field observations in the western part of the pluton, where sample AR801
267 was collected, indicate that the magmatic fabric is marked by the alignment and preferred
268 orientation of euhedral K-feldspar megacrysts that define a S1 sub-horizontal planar fabric
269 and a mineral lineation L1 O20-trending and plunging 10° (Fig. 9B), similar to D1 deformation
270 observed in the surrounding gneisses (Fig. 6 and 7). The D1 deformation is pervasive along the
271 pluton contacts and is not observed in its core (Fig. 7A). In the eastern part of the pluton, the
272 S1 foliation is deformed and reoriented by O00- to O20-striking D2 vertical structures (Fig. 6
273 and 7). In this area, K-feldspar megacrysts are deformed as well as the surrounding matrix (Fig.
274 9C). K-feldspar grains are fractured and no myrmeckite was observed. The quartz grains show
275 undulose extinction and recrystallization by bulging grain boundaries.

276 The sample AR865 comes from the core of the Montées-Pélissier pluton, which is a fine-
277 grained monzogranite that intruded the Visean metasedimentary rocks in the Servoz syncline
278 (Fig. 1 and 7B). In the whole pluton and in our sample, the magmatic assemblage is pervasively
279 deformed by the D2 such that any magmatic fabric that may have existed is not preserved. In
280 thin-section, feldspar crystals are oriented sub-parallel with the C2 shear bands and show
281 common extensive microfractures filled by quartz (Fig. 9D).

282 The Vallorcine granite (AR37) is a NE-SW-trending elongate pluton located in the north-
283 eastern part of the AR massif in the EBSZ (Fig. 1B and 3). This granite crosscuts the C'2 shear
284 bands near the Lac Emosson (Fig. 9E). The sample commonly possesses a magmatic foliation
285 defined by biotite and feldspar sub-parallel to the C'2 orientation (Joye, 1989; Bussy et al.,

286 2000). At the microscale, in sample AR73, feldspar is undeformed and quartz is nested with
287 undulose extinction and shows grain boundary migration in quartz (Fig. 9E). Local millimeter
288 shear bands are associated to subgrain rotation recrystallization in quartz.

289 The Monteners granite (MB43) intruded paragneiss and orthogneiss migmatites of the MB
290 massif (Fig. 1B and 3A). The Monteners granite and its host rocks are strongly deformed
291 within an anastomosed network of C2 and C'2 shear zones of the MSZ (Fig. 2, 3A and 9F). In
292 sample MB43, fractures in feldspar are filled by quartz and recrystallized polygonal quartz (Fig.
293 9G). Locally, the quartz polygons are deformed within C'2 shear bands.

294 The Mont-Blanc granite (MB37) is a kilometer-large NE-SW-trending elongate pluton and
295 forms the main part of the MB massif (Fig. 1B and 3B). The pluton contacts are deformed in
296 C2 and C'2 structures whereas its core is weakly deformed. The granite shows a magmatic
297 foliation defined by the weak alignment of K-feldspar, biotite crystals and mafic enclaves
298 striking 020-040 (Bussy, 1990), sub-parallel to the C'2 shear planes (Fig. 9H).

299 4.2. *Smaller magmatic bodies*

300 Sample AR1028 comes from one of the dykes composing the Morcles microgranite, located in
301 the northern part of the AR massif (Fig 1B and 3C). This microgranite has a main NE-SW-
302 trending orientation and locally crosscuts C2 and C'2 shear zones. There is no apparent
303 preferred mineral orientation. Quartz grains do not show undulose extinction and are locally
304 nested (Fig. 9I). Calcite had partially replaced some feldspar grains and is present in cracks in
305 feldspar (Fig. 9I).

306 Pegmatites are common in the orthogneiss of the Lac Cornu area (Fig. 1B and 7D). The sample
307 AR833 is from one of these pegmatites, that has a diffuse contact with the orthogneiss

308 migmatite (Fig. 10A). The feldspars in the pegmatite are preferentially oriented parallel to the
309 C2 shear bands in the surrounding rocks (Fig. 10A). K-feldspar grains are surrounded by
310 myrmekite.

311 The sample AR1020 corresponds to a pegmatite that crosscuts the C2 planes of an amphibolite
312 lens in the Lac Cornu orthogneiss (Fig. 10B). It does not have an apparent preferred mineral
313 orientation. Quartz has weakly developed undulose extinction and recrystallization by grain
314 boundary migration.

315 The Lacs Noirs pegmatite is a ten centimeter-large dyke in paragneiss. It is affected by the D2
316 dextral wrenching and C2 shear bands are recognized (Fig. 1B and 10C). Quartz is strongly
317 deformed and well-developed undulose extinction. Tourmaline is either undeformed and
318 oriented parallel to the foliation or sub-parallel to the foliation, fractured and truncated. K-
319 feldspar is replaced by muscovite in shear bands.

320 The sample AR916 comes from an aplite dyke that emplaced within a decametric C2 shear
321 zone in metasedimentary rocks (Fig. 1B and 10D). The mineral assemblage does not have an
322 apparent preferred mineral orientation. Some plagioclase and K-feldspar are partially
323 replaced by white mica.

324

325 **5. U-Th-Pb dating of studied samples**

326 *5.1. analytic method*

327 Zircon and monazite U-Th-Pb age determinations of these samples were carried out using
328 Laser Ablation-Inductively Coupled Plasma Mass Spectrometry (LA-ICP-MS) at the Laboratoire

329 Magmas et Volcans, Clermont–Ferrand (France). Separated zircon and monazite grains were
330 mounted in epoxy resin discs that were polished to reveal equatorial cross sections.
331 Cathodoluminescence (CL) and Back-Scattered Electron (BSE) images were used to select
332 points for analysis. The analyses involve the ablation of minerals with a Resonetics Resolution
333 M-50 powered by an ultra-short pulse ATL Atlex Excimer laser system operating at a
334 wavelength of 193 nm (detailed description in Müller et al., 2009). The detailed analytical
335 procedures are described in Paquette and Tiepolo (2007), Hurai et al. (2010), and Paquette et
336 al. (2014) and detailed in the Supplementary material (S1). Data reduction was carried out
337 with the GLITTER[®] software package developed by Macquarie Research Ltd (Jackson et al.,
338 2004). The analytical data are provided in the Supplementary Material 1 (SM1). Ages and
339 diagrams were generated using the Isoplot/Ex v. 2.49 software package by Ludwig (2001). Only
340 the concordant data and the discordant data fitting with the discordia line were taken into
341 account in the age calculation. In the text and figures, all uncertainties in ages are given at \pm
342 2σ level.

343 5.2. Couteray orthogneiss (AR37)

344 Zircon grains from the Couteray orthogneiss are transparent and euhedral with a shape that
345 varies from equant to elongate. CL images show either the presence of inherited
346 cores surrounded by rims with concentric oscillatory zones, or uniform grains also with
347 concentric oscillatory zones (Fig. 11A). Twenty-eight analyses were conducted on seventeen
348 zircon crystals (Fig. 12A; Table S1). Analyses of inherited cores with concentric zones and Th/U
349 ratios between 0.18 and 0.99 (Table S1) yield one concordant date at 691 Ma (#12) and a
350 cluster of five data (#8, 10, 18, 20, 25) giving a concordia age of 587 ± 10 Ma ($MSWD_{(C+E)} =$
351 1.16) (Fig. 12A). Nineteen analyses on cores and rims with concentric zones and Th/U ratios

352 ranging between 0.01 and 0.76 (Table S1) yield a concordia age at 480 ± 4 Ma ($MSWD_{(C+E)} =$
353 0.61, $n = 19$) (Fig. 12A).

354 5.3. Early Carboniferous (Visean) granites (ca. 340-330 Ma).

355 5.3.1. The Pormenaz granite (AR801)

356 Most of the zircon grains analysed are euhedral, either prismatic with a shape ratio up to 2:1
357 or stubbier with a shape ratio of 1:1 (Fig. 11B). They are pinkish, transparent to slightly opaque.
358 CL images show strong evidence of concentric or oscillatory igneous growth zones as well as
359 the presence of cores displaying either sector-like or patchy zone textures surrounded by
360 zoned rims (Fig. 11B). Seventy-five analyses were performed on sixty-five zircon crystals (Table
361 S1). In the Tera Wasserburg diagram, excepting from two cores (#10 and 35) concordant
362 around 650 Ma, all data are scattered along the concordia curve between around 340 to 190
363 Ma with thirty-two data yielding a concordia age of 338 ± 2 Ma ($MSWD_{(C+E)} = 1.4$) (Fig. 12B).
364 These data are mainly obtained on zoned cores (24 cores and 8 rims). The analysed grains
365 have a range of Pb (8.5-69 ppm), Th (most 55-281 ppm) and U (150-1526 ppm) contents and
366 Th/U ratios (most 0.15-0.51) (Table S1). Other discordant data (dotted ellipses) mainly
367 composed of rims (34 rims and 7 cores) are characterized by similar Pb, Th and U contents
368 (17-75 ppm, 64-458 ppm and 351-2027 ppm) and Th/U ratios (most 0.14-0.66) (Table S1).
369 These data are not taken into consideration for the age calculation because they are
370 discordant. These discordances are probably due to radiogenic Pb losses and common Pb
371 contaminations.

372 5.3.2. The Montées-Pélissier granite (AR865)

373 Zircon crystals from sample AR865 are pinkish, transparent, euhedral and elongate but
374 commonly broken. CL images show strong evidence of concentric or oscillatory igneous
375 growth zones (Fig. 11C). Forty-three analyses are obtained on rims or cores of 43 crystals and
376 present Th/U ratios ranging between 0.04 and 1.02 (most 0.16-0.67) with homogeneous Pb
377 content (most 21-64 ppm) and variable U (most 555–1450 ppm) and Th (most 90–347 ppm)
378 contents (Table S1). In the Tera Wasserburg, the data are scattered along the concordia curve
379 between around 350 to 210 Ma (Fig. 12C). The eight oldest data (#2, 6, 7, 8, 12, 13, 22 and 34)
380 form a cluster around 340-335 Ma that yields a concordia age of 340 ± 5 Ma ($MSWD_{(C+E)} = 2.2$).
381 Other data (dotted ellipses), often discordant, show younger $^{206}\text{Pb}/^{238}\text{U}$ dates (Table S1; Fig.
382 12C). These data are not considered because they were probably affected by radiogenic Pb
383 losses as well as common Pb contaminations.

384

385 *5.4. Late Carboniferous granite (ca. 305 Ma)*

386 *5.4.1. Vallorcine granite (AR73)*

387 The zircon crystals from the Vallorcine granite (AR73) are transparent, pinkish and euhedral.
388 Zircon ranges in shape from equant to elongate. The latter are commonly fractured. CL images
389 show complex internal textures such as the presence of apparently inherited cores and
390 concentric oscillatory and patchy zones textures (Fig. 11D). Twenty-nine analyses were carried
391 out on twenty-two zircon crystals (Fig. 12D). Two data from two cores (#4 and 25) are sub-
392 concordant and yield an upper intercept at 2071 ± 75 Ma in the concordia diagram. These
393 zircon cores have similar Pb (64-67 ppm), Th (31-59 ppm) and U (181-184 ppm) contents with
394 Th/U ratios of 0.17 and 0.32 (Table S1). Three data obtained on cores show Th/U ratios of ca.

395 0.3 and are sub-concordant around 650 Ma (#15 and 20) and 840 Ma (#2) (Table S1). The other
396 twenty-four data are scattered along the concordia curve between ca. 840 to 220 Ma in two
397 main distinct clusters: one very wide between 485 and 450 Ma (group 1) and the other more
398 restricted between 310 to 300 Ma (group 2). Group 1 dates (#3, 5, 6, 10, 12, 18, 22) were
399 determined from 5 cores and 2 rims. These seven analyses are characterized by variable Pb
400 and Th contents ranging from 19 to 52 ppm and 11 to 183 ppm, respectively and by Th/U
401 ratios from 0.04 to 0.54 (most 0.13-0.54) (Table S1). The linear regression on these seven data
402 yields a lower intercept of 468 ± 13 Ma (MSWD = 2). Amongst these data, six give a concordia
403 age of 469 ± 12 Ma (MSWD_(C+E) = 2.6). Group 2 dates (#7, 8, 11, 16, 19, 21, 23, 26, 27, 29) are
404 obtained from 2 cores and 8 rims. Pb and Th contents ranging from 12-72 ppm and 11-201
405 ppm, respectively, and with Th/U ratios from 0.01 to 0.31 (most 0.1-0.31). These ten data yield
406 a concordia age of 306 ± 5 Ma (MSWD_(C+E) = 1.8). Five data (white ellipses) between these two
407 clusters may correspond to a mixed age. The two youngest data (dotted ellipses) may be the
408 result of radiogenic Pb loss.

409 5.4.2. Montenvers granite (MB43)

410 Zircon crystals from sample MB43 are pinkish and transparent. They are either equant with a
411 shape ratio up to 2:1 or in the form of prismatic or elongate grains. CL images show concentric
412 or oscillatory igneous growth zones as well as the presence of cores displaying either sector-
413 like or patchy zones textures surrounded by zoned rims with locally a thinner and CL-dark
414 over-rim (Fig. 11E). Forty-five analyses are obtained on rims or cores of 40 crystals and present
415 Th/U ratios ranging between <0.01 and 1.30 (most 0.01-0.82) with variable Pb (3.3-404 ppm),
416 U (most 98–5721 ppm) and Th (most 29–869 ppm) compositions (Table S1). In the Tera
417 Wasserburg diagram, excepting datum #4 (not plotted) measured on the inherited core of the

418 zircon Z9 with a Th/U ratio of 1.30 and a discordant position around 1.8 Ga, all other data are
419 scattered along the concordia curve between ~620 to 220 Ma in a cluster around 310-220 Ma
420 and two others more restricted around 600 Ma and 450 Ma (Fig. 12E). The cores of zircons
421 Z10 (#9) and Z19 (#19) have a Th/U ratio of 0.32 and 0.79 and give concordant data at $615 \pm$
422 16 Ma and 592 ± 16 Ma, respectively. The cluster at 450 Ma consisting of the analyses obtained
423 on three tips (#1, 35, 43; Th/U = 0.01-0.26) and two cores (#29, 37; Th/U = 0.15-0.38) yields a
424 concordia age of 447 ± 10 Ma ($\text{MSWD}_{(C+E)} = 1.6$, $n = 4$). Among the thirty-eight youngest data,
425 nineteen data from 10 cores and 9 rims yield a concordia age of 306 ± 3 Ma ($\text{MSWD}_{(C+E)} = 1.6$)
426 (Fig. 12E). In the diagram, the dotted ellipses are obtained mainly on the metamict CL-dark
427 rim and are characterized by very high U contents (1315-9763 ppm).

428 5.4.3. Mont-Blanc granite (MB37)

429 The zircon crystals from the Mont Blanc granite (MB37) are transparent, pinkish and euhedral
430 with an elongate shape with a shape ratio up to 3:1. CL images show oscillatory igneous
431 growth zones as well as the presence of few cores displaying either sector-like zones
432 surrounded by CL-dark zoned rims (Fig. 11F). Forty-three analyses were carried out from forty-
433 two zircons (Fig. 12F; Table S1). Among them, two are (#15 and 34) composed by cores
434 characterized by concentric zones and a Th/U ratio of 0.34, and are concordant at ca. 485 Ma
435 and ca. 558 Ma. There are two more data (#1 and 10) obtained on a core and a rim with a
436 Th/U around 0.3-0.4, that are concordant at ca. 335 Ma. Otherwise, thirty-five data plot as a
437 cluster characterized by Th/U ratios ranging between 0.2 and 0.86 and yield a concordia age
438 of 305 ± 2 Ma ($\text{MSWD}_{(C+E)} = 1.5$, $n = 35$). Two discordant data (dotted ellipses) (#37 and 42)
439 obtained on CL-dark rims show youngest $^{206}\text{Pb}/^{238}\text{U}$ dates, which may be the result of
440 radiogenic Pb loss as well as common Pb contamination.

441 5.5. *Smaller granitic bodies (e.g. microgranite, aplite and pegmatite dykes)*

442 5.5.1. *Morcles microgranite (AR1028)*

443 Zircon crystals from sample AR1028 are colourless to slightly pink and transparent. They are
444 either prismatic with an shape ratio up to 3:1, or ovoid, but also sometimes as fragment-like.
445 CL images show complex internal features such as the presence of cores and concentric
446 oscillatory and patchy zones textures (Fig. 13A). Some crystals have metamict rims, which
447 could not be analysed because they are too rich in common Pb. Monazite crystals were found
448 in this sample. They are light yellow, transparent and euhedral. EBS images exhibit concentric
449 oscillatory or patchy zones (Fig. 13A).

450 Twenty analyses on seventeen zircon crystals yield Th/U ratios ranging between 0.08 and 0.62
451 (most 0.1-0.44) with variable Pb (3.9-118 ppm), U (40–2298 ppm) and Th (16–731 ppm)
452 contents (Table S1). In the Tera Wasserburg diagram, excepting data 5 and 8, the concordant
453 to sub-concordant data are scattered between ca. 800 and ca. 450 Ma (Fig. 14A). The linear
454 regression on ten data (#1, 4, 6, 9, 10, 11, 14, 16, 17, 18) obtained on 5 cores and 5 rims yields
455 a lower intercept of 463 ± 10 Ma (MSWD = 2.9 Ma). Sixteen analyses were also performed on
456 nine monazite crystals (Table S1). Excepting the analysis #11, data form a cluster with a
457 concordia age of 313 ± 2 Ma (MSWD_(C+E) = 0.49, n = 15) (Fig. 14B). Spot #11, that has a
458 discordant position around ca. 360 Ma may correspond to an analytical mixture.

459 5.5.2. *Lac Cornu pegmatites (AR833 and AR1020)*

460 Zircon crystals from sample AR833 are euhedral, colourless and transparent. Their shapes are
461 either elongate or rounded. CL images highlight various cores surrounded by rims with
462 concentric and oscillatory zones (Fig. 14B). Sixty-three analyses on forty-three zircon grains

463 are distributed into four clusters (Fig. 14C). Three data (#15, 20, 46) from cores with Th/U
464 ratios between 0.16 and 0.23 yield a mean $^{238}\text{U}/^{206}\text{Pb}$ date at 724 ± 28 Ma (MSWD = 1.3). Four
465 data (#2, 4, 22, 34) also from cores with similar Th/U ratios (0.19-0.28) return a concordia age
466 at 552 ± 12 Ma (MSWD_(C+E) = 2.4). The main cluster is composed of fifty-one analyses from
467 cores and rims with concentric and oscillatory zones and lower Th/U ratios (mostly 0.04-0.15)
468 from ca. 465 Ma to 420 Ma. Among them, twenty-eight data yield a concordia age at 462 ± 3
469 Ma (MSWD_(C+E) = 1.08). In addition, two sub-concordant data (#45, 48) from rims with
470 oscillatory and concentric zones and low Th/U ratios (0.00-0.01) yield a mean $^{238}\text{U}/^{206}\text{Pb}$ date
471 at 317 ± 6 Ma (MSWD = 1.04). One datum (#16) from a zircon core is concordant at 2.0 Ga
472 (Table S1).

473 Zircon crystals from the pegmatite AR1020 are not common, often metamict and pinkish, or
474 transparent to milky. Their shapes vary from elongate to rounded. CL images reveal complex
475 textures such as the presence of cores surrounded by rims, concentric oscillatory and patchy
476 zones textures (Fig. 14C). Nineteen analyses were performed on eleven grains (Table S1).
477 Despite the various and complex zones of these zircon grains and their scattered Th/U ratios
478 (0.05-1.03), all the data are between ca. 465 and 375 Ma and thirteen yield a concordia age at
479 456 ± 4 Ma (MSWD_(C+E) = 0.5) (Fig. 14D). Other analyses might reflect Pb loss or common Pb
480 contamination.

481 5.5.3. Lacs Noirs pegmatite (AR1006)

482 Zircon crystals from the pegmatite specimen are colourless and transparent fragments. CL
483 images show that most of the grains have resorption structures affecting cores and rims with
484 oscillatory and concentric zones (Fig. 13D). Thirty-three analyses were performed on thirty-
485 two zircon grains (Fig. 14E). Twenty-two data with Th/U ratios ranging between 0.04 and 0.70

486 align and form a lower intercept at 455 ± 3 Ma (MSWD = 0.48). Among them, seventeen data
487 yield a concordia age at 456 ± 3 Ma (MSWD_(C+E) = 0.89). Other analyses, except one (#14), are
488 concordant or sub-concordant and spread from 535 to 997 Ma.

489 5.5.4. Chéserys aplite (AR916)

490 Zircon crystals from aplite are not common and are mainly transparent and colourless grains
491 with elongate to ovoid shapes. CL images show mainly simple internal structures with
492 concentric and oscillatory zones (Fig. 13E). A few grains show a core surrounded by a rim with
493 oscillatory zones. Some grains also display a metamorphic rim. Thirty-three analyses on thirty-
494 two zircon grains (Fig. 14F) yield a cluster between 460 and 420 Ma. Among them, eighteen
495 analyses on cores and rims with Th/U ratios between 0.04 and 0.95 yield a concordia age at
496 458 ± 3 Ma (MSWD_(C+E) = 1.3). One analysis (#22) on a core is sub-concordant at 839 Ma.
497 Several discordant data show $^{206}\text{Pb}/^{238}\text{U}$ dates younger than 400 Ma.

498

499 6. Discussion

500 6.1. Emplacement ages of granites and pegmatites

501 6.1.1. Ordovician magmatism

502 Zircon grains from the Couteray orthogneiss (AR37) yield two concordia ages: one Ordovician
503 at 480 ± 4 Ma and the other Precambrian at 587 ± 10 Ma (Fig. 12A). The first one was obtained
504 on zircon cores and rims showing oscillatory and concentric zones (Fig. 11A) typical of
505 magmatic origin (Linnemann et al., 2011; Tiepel et al., 2004); we therefore interpret it as the
506 Ordovician emplacement age of the magmatic protolith of the Couteray orthogneiss. The

507 Precambrian age was obtained on zircon cores that are locally partially resorbed (Fig. 11A,
508 Zr36). The Precambrian one was obtained on zircon cores that are locally partially resorbed
509 (Fig. 11A, Zr36). The geological significance of this inherited precambrian age remains
510 unknown.- The Ordovician age is slightly older than the magmatic protolith emplacement ages
511 of other orthogneisses from the AR and MB massifs dated between 465 and 455 Ma (Bussy
512 and von Raumer, 1994; Bussy et al., 2011) (Fig. 1B). However, this age remains consistent with
513 the 480-450 Ma age range proposed for the Ordovician magmatic event that is well-
514 documented throughout the Variscan belt (Melleton et al., 2010 and references therein;
515 Lotout et al., 2017; Chelle-Michou et al., 2017).

516 *6.1.2. Early Carboniferous plutonism (ca. 340-330 Ma)*

517 Most of the zircon grains analysed from the Pormenaz (AR801) and Montées-Pélissier (AR865)
518 granites show magmatic growth zones with Th/U ratios from 0.1 to 1.0 typical of an igneous
519 zircon origin (Tiepel et al., 2004; Linnemann et al., 2011) (Fig. 11B and C; Table S1). The zircon
520 concordia ages of 338 ± 2 Ma and 340 ± 5 Ma obtained on these two plutons match within
521 uncertainties and are interpreted as emplacement ages (Fig. 12B and C). These results agree
522 with the ages at 332 ± 2 Ma and 331 ± 2 Ma documented by Bussy et al. (2000), and therefore
523 confirm the occurrence of an Early Carboniferous (Visean) magmatism in the AR massif (Fig.
524 1B). Moreover, these two samples yield discordant data, mainly obtained on zircon rims,
525 which are probably affected by radiogenic Pb losses during the successive Variscan and Alpine
526 tectono-metamorphic events.

527 *6.1.3. Late Carboniferous plutonism*

528 The concordia ages of 306 ± 5 Ma, 306 ± 3 Ma and 305 ± 2 Ma on the Vallorcine (AR73),
529 Montenvers (MB43) and Mont-Blanc granites (MB37), respectively, are from zircon cores and
530 rims showing concentric and oscillatory zones with Th/U ratios mostly higher than 0.1 typical
531 of igneous zircons (Tiepel et al., 2004; Linnemann et al., 2011) (Fig. 11D-F and 12D-F; Table
532 S1). These dates are interpreted as emplacement ages and are consistent with previous
533 published ID-TIMS U-Pb ages on zircon and monazite at ca. 305 Ma for these same plutons
534 (Bussy et al., 2000; Bussy and von Raumer, 1993, 1994) (Fig. 1).

535 In this study, most of the concordant data obtained on zircon from the felsic dykes (AR1028,
536 AR833, AR1020, AR1006 and AR916) range from ca. 465 to 455 Ma (Fig. 14; cf section 5.2).
537 Field-work shows that these felsic dykes emplaced contemporaneously with dextral shearing
538 during Carboniferous times (Bussy and von Raumer, 1994; von Raumer and Bussy, 2004; Fig.
539 10). Therefore, the Ordovician record reflects the presence of an inherited component
540 associated with an Ordovician magmatic event at ca. 465-455 Ma.

541 Zircon and monazite U-Th-Pb dating of the Morcles microgranite (sample AR1028) yielded two
542 distinct concordia ages, one at 313 ± 2 Ma and the other at 463 ± 10 Ma (Fig. 14A and B). The
543 younger one was determined on euhedral monazite grains showing concentric growth zones,
544 and is similar to the zircon LA-ICPMS U-Th-Pb age at ca. 312-309 Ma obtained for one of the
545 magmatic pulses proposed for the Morcles microgranite dykes in Bussien et al. (2017).
546 Therefore, we interpret the monazite concordia age at 313 ± 2 Ma as the emplacement age of
547 the AR1028 microgranite dyke and the zircon concordia age at 463 ± 10 Ma as the age of an
548 inherited Ordovician component, which was identified in Bussien et al. (2017) too.

549 Moreover, two zircon grains from the Lac Cornu pegmatite AR833 show two sub-concordant
550 analyses at ca. 317 Ma (Fig. 14C). These analyses were obtained on zircon rims with oscillatory

551 and concentric zones and low Th/U ratios (0.00-0.01; Table S1), which is characteristic of
552 magmatic zircon that may have originated from high-SiO₂ and/or peraluminous granitoids
553 (Lopez-Sanchez et al., 2016). This mean at 317 ± 6 Ma might represent the emplacement age
554 of the pegmatite AR833 and would be consistent with the emplacement age of the Morcles
555 microgranite at 312 ± 2 Ma and the 317 ± 3 Ma age proposed for the anatectic leucogranitic
556 dykes of the Mont-Blanc massif (Bussy and von Raumer, 1994). However, given the small
557 number of data ($n = 2$), we cannot exclude that these two analyses are be the result of a
558 mixture between an Ordovician component and a younger component either Late
559 Carboniferous (~ 305 Ma), Permo-Triassic or even Tertiary in age.

560

561 *6.2. Zircon inheritance and source of Carboniferous magmas*

562 Most of magmatic bodies we studied (i.e., microgranitic, pegmatitic and aplitic dykes) show
563 zircon grains that do not record their age of emplacement (Carboniferous). Our results from
564 zircon crystals from the Morcles microgranitic dyke show a well-marked Ordovician
565 inheritance at 463 ± 10 Ma (Caledonian event) and minor Ediacaran contributions (Pan-African
566 event) (Fig. 14A) as already suggested in Bussien et al. (2017). The zircon U-Th-Pb ages from
567 the Lac Cornu (AR833 and AR1020) and Lacs Noirs (AR1006) pegmatites and the Chéserys
568 aplite (AR920) also yielded similar Ordovician ages at 462 ± 3 Ma, 456 ± 4 Ma, 455 ± 3 and 458
569 ± 3 Ma, respectively. This ca. 460-450 Ma inheritance was obtained on zircon grains
570 characterized by concentric growth zones and high Th/U ratios typical of an igneous origin
571 (Tiepel et al., 2004; Lineman et al., 2011) (Fig. 13; Table S1).

572 In granitic magmas, inherited zircon crystals originate from the melted sources (Bea et al.,
573 2021). Thus, the important Ordovician inheritance recorded by the zircon crystals of the
574 smaller magmatic bodies argues for a genetic link between these intrusions and the partially
575 molten Ordovician orthogneisses. Such hypothesis of orthogneisses as being the main source
576 for silicic melts is consistent with our field-observations of, for instance, pegmatite AR833 that
577 formed in-situ within orthogneiss migmatite (Fig. 10A) or the pervasive leucocratic vein and
578 dykes complex into the partially molten orthogneiss that surrounds the Mont Blanc granite
579 (Vitel, 1965; Bussy and von Raumer, 1994). All the smaller magmatic bodies dated in this study
580 may thus represent anatectic melt that originated from orthogneiss migmatite and that
581 crystallized during ascent (Brown, 2013 and references therein) between ca. 320-310 Ma.

582 Growth of zircon in an anatectic melt is considered to result solely from the dissolution of pre-
583 existing zircon grains and (re)precipitation of overgrowths or neograins directly from the melt
584 (Watson, 1996; Yakymchuk and Brown, 2014; Bea et al., 2006; Kelsey et al., 2008; Mintrone
585 et al., 2020). The solubility of zircon in silicate melts depends on melt temperature
586 composition (Watson and Harrison, 1983; Boehnke et al., 2013). It also depends on heating
587 and cooling rates (Bea et al., 2007), that are controlled by the shape and size of the magmatic
588 body (de Saint-Blanquat et al., 2011). In the AR and MB massifs, the range of metamorphic
589 peak temperatures estimated in the partially molten gneissic basement is about 650-750°C
590 (Schulz and von Raumer, 1993, 2011; Chiaradia, 2003; Genier et al., 2008) and rises 750-800°C
591 in the lower crust (Vanandois et al., 2022). In the middle crust, at temperatures between 650-
592 700 °C, biotite and amphibole dehydration melting is limited (e.g. Wienberg and Hasalova,
593 2015). The absence of peritectic minerals in migmatite leucosome, their low muscovite and
594 sillimanite contents and the high leucosome fraction observed in the AR and MB migmatites

595 (von Raumer and Bussy, 2004) attest for melt production through water-present melting
596 reactions (White et al., 2005; Sawyer, 2010), as previously proposed in Genier et al. (2008) for
597 migmatite of the Ecosson area. Couzinié et al. (2021) highlighted water-fluxed melting of
598 quartzo-feldspathic orthogneisses in the eastern French Massif Central. The conclusions of
599 Couzinié et al. (2021) are that low melting temperature involve limited zircon solubility in the
600 melt phase. In addition, zircon grains armoured as inclusions in non-reacting biotite prevents
601 the crystallization of newly formed zircon from the anatectic melt (Bea, 1996; Yakymchuk and
602 Brown, 2014). We propose that most of the pegmatite, aplite and microgranite in the AR and
603 MB massifs, that are characterized by important Ordovician inheritance without
604 Carboniferous zircon recrystallization, originated from water-fluxed melting of Ordovician
605 orthogneisses. Although less pronounced, the Ordovician inheritance was also recorded in
606 magmatic zircon cores in the Monteners (MB43), Vallorcine (AR73) and Mont-Blanc (MB37)
607 granites (Fig. 12D-F). These late Carboniferous granites (~305 Ma) have peraluminous
608 chemical compositions and a continental crust origin (von Raumer and Bussy, 2004). They are
609 also spatially associated to the orthogneiss migmatite (Fig. 1B; Vitel, 1965). Similarly, we
610 propose that the main melt production process at the origin of the Vallorcine, Monteners
611 and Mont-Blanc granites is water-fluxed melting of Ordovician orthogneisses. The discrete
612 presence of Ordovician inheritance in the Monteners, Vallorcine and Mont-Blanc granites
613 can be attributed to the kinetics of heat transfer in felsic magmas that impacted zircon
614 dissolution. Because of a greater volume, plutons have lower cooling rates than dykes (de
615 Saint-Blanquat et al., 2011), and have higher temperature conditions that enhance the
616 dissolution of zircon grains (Bea et al., 2007). Zircon grains of Early Carboniferous plutons
617 (AR801, AR865) show almost no inheritance (Fig. 12B and C). This could also be the result of

618 an efficient zircon dissolution process due to the metaluminous composition of magmas (Bea
619 et al., 2006) and/or higher temperature conditions (Kelsey et al., 2008).

620 The importance of Lower Paleozoic igneous rock contributions, particularly Ordovician
621 intrusions, has been widely proposed for the sources of the Late Carboniferous Variscan
622 granites in the French Central Massif (Downes and Duthou, 1988; Pin and Duthou, 1990;
623 Turpin et al., 1990; Downes et al., 1997), in the Armorican massif (Ballouard et al., 2017, 2018)
624 and in Iberia (Neiva et al., 2012; Villaseca et al., 2012; Rodriguez et al., 2022). The strong
625 contribution of meta-igneous rocks as melt sources for Late Carboniferous magmatism
626 suggests that an important part of the melt fraction produced during the Variscan orogeny
627 was generated by water-fluxed melting reactions rather than water-absent dehydration
628 melting. This interpretation is consistent with recent studies highlighting that water-fluxed
629 partial melting reactions are common phenomena in orogenic crust and are often at the origin
630 of crustal-derived magmas (i.e. peraluminous magmas) (e.g. Wienberg and Hasalova, 2015;
631 Sawyer et al., 2011). The water supply may originate from different sources such as water
632 coming from the dehydration of nearby metapelitic rocks (Sawyer, 2010; White et al., 2005;
633 Weinberg and Hasalová, 2015) or from the lower crust (Braga and Massone, 2012).

634 Mafic enclaves are found in the Mont-Blanc pluton (Bussy, 1990) and several ca. 307 Ma old
635 mafic intrusions have also been documented in the Fully area (Bussy et al., 2000) arguing for
636 a contribution of a mantle source in the Late Carboniferous magmatism. Similarly, based on
637 their geochemical signatures, von Raumer and Bussy (2004) suggested that the Montées-
638 Pélissier and Pormenaz plutons probably originated from partial melting of the overthickened
639 lower crust and interpreted enclaves of durbachites and lamprophyres as evidence of a mantle
640 source. Early Carboniferous plutons also described in other ECMs (e.g. Schaltegger and Corfu,

641 1992; Debon et al., 1994, 1998; Guerrot and Debon, 2000; Rubatto et al., 2001) show similar
642 geochemical compositions and are also interpreted as a mixing between crustal and mantle
643 sources (Debon and Lemmet, 1999 and reference therein). Granite emplacement with a major
644 mantle component and dated between 340-330 Ma is also known in other Variscan massifs
645 (e.g., Vosges: Guillot et al., 2020; Tabaud et al., 2015; Corsica: Paquette et al., 2003; Li et al.,
646 2014). These similarities suggest that a mantle thermal anomaly may have affected a large
647 part of the Variscan belt and may have contributed into the bulk heat budget of the
648 continental crust. The significance of the two successive thermal anomalies (i.e. Early and Late
649 Carboniferous) associated with the two magmatic pulses in the AR and MB massifs and others
650 ECMs remains elusive. Several orogenic-scale geodynamic events have been proposed, such
651 as delamination of the lithospheric mantle (e.g. Laurent et al., 2017; Vanderhaeghe et al.,
652 2020), mantle plume (Franke, 2014) or sub-lithospheric relamination and magmatic flow as
653 recently invoked in the Bohemian massif (Maierova et al., 2018, 2021).

654

655 *6.3. Melt drainage during crustal-scale shear zone evolution*

656 Based on structural and geochronological data, we propose a temporal evolution of the
657 tectono-magmatic system during Carboniferous transpression. This conceptual model
658 emphasizes the role of anastomosed shear zone network growth and water-fluxed melting of
659 orthogneisses (Fig. 15). In the AR and MB massifs, the Variscan magmatism started around
660 340-330 Ma with the emplacement of the Pormenaz and Montées-Péllissier granites (Fig. 12B
661 and C; Bussy et al., 2000). This magmatic pulse occurred in an overthickened crust as
662 documented by the pressure conditions at ca. 1.75 GPa recorded in the eclogites and dated at
663 340-330 Ma (Vanardois et al., 2022). These two Early Carboniferous granites were emplaced

664 at upper crustal levels. The root zone of plutons is not exposed and the feeder structures are
665 unknown. Our observations argue for a subsolidus deformation with the development of S2
666 and C2 structures. In addition, microstructures show fractured K-feldspar grains without
667 myrmekite formation and bulging recrystallization in quartz (Fig. 9C and D), suggesting a
668 subsolidus deformation (Passchier and Trouw, 2005). The magmatic foliation and lineation in
669 the western side of the Pormenaz granite show sub-parallel orientation to the D1 deformation
670 in the surrounding rocks and can be interpreted as syn-D1. Alternatively, the Montées-
671 Pélissier granite displays microfractures in plagioclase healed by quartz (Fig. 9D), which is
672 typical of submagmatic deformation (Bouchez et al., 1992; Pawley and Collins, 2002), and
673 plagioclase porphyroblasts are oriented sub-parallel to the S2 and C2 structures. These
674 features may indicate an emplacement through vertical shear zones during the D2
675 transpression (Fig. 15A) and a subsolidus deformation during the ongoing D2 transpression.
676 Therefore, we propose that the vertical dextral shear zones may have initiated at 340-330 Ma
677 with limited upward transfer of fluids and melts from the lower crust to upper crustal levels
678 (Fig. 15A). Similar ages for the beginning of the dextral transpression are documented in the
679 Argentera massif (Simonetti et al., 2018, 2021). Vanardois et al. (2022) proposed that D1
680 initiated after the peak of pressure at ca. 340-330 Ma and interpreted D1 as a record of
681 longitudinal flow of the partially molten lower crust. Based on the similar ages of the
682 Pormenaz and Montées-Pélissier granites interpreted as syn-D1 and syn-D2 plutons,
683 respectively, our results suggest that the initiation of D2 transpression is coeval with this D1
684 longitudinal flow. The similar stretching direction (330-040) recorded by L1 and L2 lineations
685 are consistent with the concomitant D1 deformation longitudinal flow and the onset of D2
686 transpression. Similar partitioning of the deformation between horizontal and vertical fabrics

687 during longitudinal flow has been described in the Variscan belt (e.g. Cochelin et al., 2021) and
688 in others hot orogens (e.g. Gapais et al., 2005; Yin and Taylor, 2011; Xu et al., 2015).

689 Ongoing dextral transpression is responsible for the development of a regional-scale
690 anastomosed shear zone network with a S-C-C'-like structure. Numerous felsic dykes and
691 pegmatites located in the C2 shear zones show evidences of syn-kinematic emplacements as
692 exemplified by diffuse contact with the C2 migmatite layers (Lac Cornu pegmatite; Fig. 10A)
693 or typical S-C structures (Lacs Noirs pegmatite; Berthé et al., 1979) (Fig. 10C). These dykes are
694 dated between 310-320 Ma (Fig. 14B and C), similar to the 317 ± 2 Ma age of leucogranitic
695 injections in dextral shear bands documented in the MB massif (Bussy and von Raumer, 1994).
696 These ages are also consistent with the dextral shearing constrained at ca. 320 Ma in the EBSZ
697 (Simonetti et al., 2020). We propose that the formation and broadening of these shear zones
698 enhanced aqueous fluid drainage in the orthogneisses and, thus, increased the water-fluxed
699 melting reaction (Fig. 15B). The anatectic melts were collected in the C2 shear zones and
700 formed the syn-kinematics dykes (Fig. 10 and 15B).

701 The Vallorcine granite crosscuts C'2 shear bands (Fig. 9E). The granite also shows magmatic
702 planar fabrics sub-parallel to the C'2 structures (Bussy et al., 2000) and a weakly developed
703 subvertical foliation in surrounding granitic dykes (Simonetti et al., 2020). Therefore, the
704 emplacement of this granite is syn-C'2. A similar magmatic fabric in the core of the Mont-Blanc
705 granite also indicates a syn-C'2 emplacement. The Montenvers granite has recorded quartz-
706 polygonal recrystallization typical of high-temperature deformation (Passchier and Trouw,
707 2005) and fracture in plagioclase healed by quartz indicating submagmatic deformation
708 (Bouchez et al., 1992; Pawley and Collins, 2002) (Fig. 9G), whereas deformation of quartz in
709 shear bands emphasizes lower-temperature deformation (Fig. 9G). Our structural and

710 microstructural analyses indicate that the emplacements of the Vallorcine, Montenvers and
711 Mont-Blanc granites took place inside crustal dextral C'2 shear zones (Fig. 2 and 9E to H) and
712 no compressive structures are observed in their country rocks. Therefore, we interpret the
713 C'2-dominant domains (i.e. the EBSZ and MSZ) as large-scale dilation shear structures that
714 enhanced the emplacement of large volumes of melts within the continental crust at ca. 305
715 Ma (Fig. 15C). The C'2 shear zones represent the last structures of the dextral transpressional
716 system. This interpretation is also consistent with the occurrence of cordierite-bearing
717 migmatites in the Fully area showing cordierite clots parallel to C'2 plans (Fig. 5D) indicating a
718 syn-C'2 partial melting dated at ca. 307 Ma (Bussy et al., 2000). We speculate that local D3
719 deformation observed in the upper structural levels in the Servoz syncline may represent a
720 limited vertical thinning due to these dilation structures or to the upward movements and
721 emplacements of plutons. This deformation phase is not shown in figure 15.

722 These structural and geochronological results document a progressive growth of an
723 anastomosed shear zone network at the scale of the AR and MB massifs during the same large-
724 scale transpressional deformation. The formation of this anastomosed network started with
725 the progressive nucleation of the S2 foliation and C2-dominant shear zones at ca. 340-330 Ma.
726 The development and broadening of the anastomosed shear zone network occurred between
727 ca. 330-310 Ma. The formation of two large-scale dilation C'2 zones occurred at the end of
728 the transpression at ca. 305 Ma.

729

730 **7. Conclusion**

731 Our bulk structural analysis on the Variscan crust at the scale of the Aiguilles-Rouges and
732 Mont-Blanc massifs highlights a crustal scale S-C-C' anastomosed network formed during
733 dextral transpression along the EVSZ closely associated to plutons ascent and emplacement.
734 Zircon and monazite LA-ICPMS U-Th-Pb dating of syn-tectonic dykes and large plutons
735 constrain this bulk continental dextral deformation between ca. 340 and 305 Ma. During this
736 time span, the transcurrent EVSZ network broadened and formed a regional-scale
737 anastomosed system enhancing vertical flow and where C'-type shear zones acted as dilation
738 structures that guided the ascent and the preferential growth of plutons. Zircon inheritance
739 indicates that Late Carboniferous granitic melts are mainly derived from water-fluxed melting
740 of Ordovician orthogneiss with the input of mantle-source derived magmas. Over time, the
741 growth of the dextral anastomosed network enhanced water transfer through the shear zones
742 and water-fluxed melting to produce more anatexitic melts.

743

744 **Acknowledgements**

745 We dedicate this paper to the memory of our colleague and friend Jean-Louis Paquette who
746 sadly passed away in June 2022. His research works significantly contributed to enhance the
747 knowledge on the orogenic evolution, especially for the Variscan cycle. This work was
748 supported by the BRGM through the Référentiel Géologique de la France program (RGF). We
749 thank Cyprien Astoury for mineral separation. Didier Convert provided generous support with
750 thin section preparation. The newly acquired and compiled structural data is available on the
751 RGF website (<http://rgf.brgm.fr>).

752

753 **References**

- 754 Ballèvre, M., Manzotti, P., Dal Piaz, G.V., 2018. Pre-Alpine (Variscan) inheritance: A key for
755 the location of the future Valaisan Basin (Western Alps). *Tectonics* 37, 786–817.
- 756 Ballouard, C., Poujol, M., Boulvais, P., Zeh, A., 2017. Crustal recycling and juvenile addition
757 during lithospheric wrenching: the Pontivy-Rostrenen magmatic complex, Armorican Massif
758 (France), Variscan belt. *Gondwana Research* 49, 222–247.
759 <https://doi.org/10.1016/j.gr.2017.06.002>
- 760 Ballouard, C., Poujol, M., Zeh, A., 2018. Multiple crust reworking in the French Armorican
761 Variscan belt: implication for the genesis of uranium-fertile leucogranites. *International
762 Journal of Earth Sciences* 107 (7), 2317–2336. <https://doi.org/10.1007/s00531-018-1600-3>.
- 763 Bea, F., 1996. Residence of REE, Y, Th and U in granites and crustal protoliths; implications
764 for the chemistry of crustal melts. *Journal of Petrology*, 37(3), 521-552.
- 765 Bea, F., Montero, P., Ortega, M., 2006. A LA-ICP-MS evaluation of Zr reservoirs in common
766 crustal rocks: Implications for Zr and Hf geochemistry, and zircon-forming processes.
767 *Canadian Mineralogist* 44, 693–714.
- 768 Bea, F., Montero, P., Gonzalez-Lodeiro, F., Talavera, C., 2007. Zircon inheritance reveals
769 exceptionally fast crustal magma generation processes in central Iberia during the Cambro-
770 Ordovician. *Journal of Petrology* 48, 2327-2339.
- 771 Bea, F., Morales, I., Molina, J. F., Montero, P., & Cambeses, A., 2021. Zircon stability grids in
772 crustal partial melts: Implications for zircon inheritance. *Contributions to Mineralogy and
773 Petrology*, 176(3), 1-13.

- 774 Bellahsen, N., Mouthereau, F., Boutoux, A., Bellanger, M., Lacombe, O., Jolivet, L., Rolland,
775 Y., 2014. Collision Kinematics in the Western External Alps. *Tectonics* 33, 1055-1088.
776 <https://doi.org/10.1002/2013TC003453>.
- 777 Bellière, J., 1958. Contribution à l'étude pétrogénétique des schistes cristallins du massif des
778 Aiguilles Rouges. *Annales de la Société Géologique Belge* 81, 1–198.
- 779 Bellière, J., Streef, M., 1980. Roches d'âge viséen supérieur dans le massif des Aiguilles
780 Rouges (Haute-Savoie). *Comptes Rendus de l'Académie des Sciences de Paris* 290, 1341-
781 1343.
- 782 Berthé, D., Choukroune, P., Gapais, D., 1979. Orientations préférentielles du quartz et
783 orthogneissification progressive en régime cisailant : L'exemple du cisaillement sud
784 armoricain, *Bulletin de Minéralogie* 102, 265-272.
- 785 Boehnke, P., Watson, E.B., Trail, D., Harrison, T.M., Schmitt, A.K., 2013. Zircon saturation
786 revisited. *Chemical Geology* 351, 324–334.
- 787 Bouchez, J.L., Delas, D., Gleizes, G., Nedelec, A., Cuney, M., 1992. Submagmatic
788 microfractures in granites. *Geology* 20, 35–38.
- 789 Boutoux, A., Bellahsen, N., Nanni, U., Pik, R., Verlaguet, A., Rolland, Y., Lacombe, O., 2016.
790 Thermal and Structural Evolution of the External Western Alps: Insights from (U–Th–Sm)/He
791 Thermochronology and RSCM Thermometry in the Aiguilles Rouges/Mont Blanc Massifs.
792 *Tectonophysics* 683, 109-123. <https://doi.org/10.1016/j.tecto.2016.06.010>.
- 793 Braga, R., Massonne, H.-J., 2012. H₂O content of deep-seated orogenic continental crust: the
794 Ulten Zone, Italian Alps. *International Geology Review* 54, 633–641.

- 795 Brown, M., 2013. Granite: From genesis to emplacement. *Bulletin of the Geological Society*
796 *of America* 125, 1079–1113.
- 797 Brown, M., Solar, G.S., 1998. Shear-zone systems and melts: feedback relations and self-
798 organization in orogenic belts. *Journal of Structural Geology* 20, 211-227.
- 799 Brun, J.P., Pons, J., 1981. Strain patterns of pluton emplacement in a crust undergoing non-
800 coaxial deformation, Sierra Morena, southern Spain. *Journal of Structural Geology* 3, 219-
801 229, 1981.
- 802 Bussien Grosjean, D., Meisser, N., May-Leresche, S., Ulianov, A., Vonlanthen, P., 2017. The
803 Morcles microgranite (Aiguilles Rouges, Swiss Alps): Geochronological and geochemical
804 evidences for a common origin with the Vallorcine intrusion. *Swiss Journal of Geosciences*
805 110, 35–49. <https://doi.org/10.1007/s00015-017-0282-3>
- 806 Bussy, F., 1990. Pétrogenèse des enclaves micro-grenues associées aux granitoïdes calco-
807 alcalins: Exemple des massifs varisques du Mont-Blanc (Alpes occidentales) et miocène du
808 Monte Capanne (Ile d'Elbe, Italie). *Mémoires de Géologie de Lausanne* 7, 1–309.
- 809 Bussy, F., von Raumer, JF., 1993. U–Pb dating of Paleozoic events in the Mont-Blanc
810 crystalline massif, Western Alps. *Terra Nova* 5, 382.
- 811 Bussy, F., von Raumer, JF., 1994. U–Pb geochronology of Palaeozoic magmatic events in the
812 Mont-Blanc Crystalline Massif, Western Alps. *Schweizerische Mineralogische und*
813 *Petrographische Mitteilungen* 74, 514–515.
- 814 Bussy, F., Hernandez, J., von Raumer, JF., 2000. Bimodal magmatism as a consequence of the
815 post-collisional re-adjustment of the thickened Variscan continental lithosphere (Aiguilles

- 816 Rouges/Mont-Blanc Massifs, western Alps). Transactions of the Royal Society of Edinburgh
817 91, 221–233. doi:10.1017/S0263593300007392.
- 818 Bussy, F., Péronnet, V., Ulianov, A., Epard, J.L., von Raumer, J., 2011. Ordovician magmatism
819 in the External French Alps: witness of a peri-Gondwanan active continental margin. In
820 Gutiérrez-Marco, J.C., Rábano, I., and García-Bellido, D., eds., The Ordovician of the World:
821 Madrid, Instituto Geológico y Minero de España, Cuadernos del Museo Geominero, v. 14, p.
822 75–82.
- 823 Capuzzo, N., Bussy, F., 2000. High-precision dating and origin of synsedimentary volcanism in
824 the late Carboniferous Salvan-Dorenaz basin (Aiguilles-Rouges Massif, western Alps):
825 Schweizerische Mineralogische und Petrographische Mitteilungen 80, 147–167.
- 826 Capuzzo, N., Wetzell, A., 2004. Facies and basin architecture of the late Carboniferous Salvan-
827 Dorenaz continental basin (western Alps, Switzerland/France). Sedimentology 51, 675–697.
828 doi:10.1111/j.1365-3091.2004.00642.x.
- 829 Carosi, R., Montomoli, C., Iaccarino, S., Benetti, B., Petroccia, A., Simonetti, M., 2022.
830 Constraining the Timing of Evolution of Shear Zones in Two Collisional Orogens: Fusing
831 Structural Geology and Geochronology. Geosciences, 12(6), 231.
- 832 Chelle-Michou, C., Laurent, O., Moyen, J.F., Block, S., Paquette, J.L., Couzinié, S., Gardien, V.,
833 Vanderhaeghe, O., Villaros, A., Zeh, A., 2017. Pre-Cadomian to late-Variscan odyssey of the
834 eastern Massif Central, France: formation of the West European crust in a nutshell.
835 Gondwana Research 46, 170–190

- 836 Chiaradia, M., 2003. Formation and Evolution Processes of the Salanfe W–Au–As-Skarns
837 (Aiguilles Rouges Massif, Western Swiss Alps). *Mineralium Deposita* 38, 154-68.
838 <https://doi.org/10.1007/s00126-002-0296-1>.
- 839 Clemens, J. D., Stevens, G., 2015. Comment on 'Water-fluxed melting of the continental
840 crust: A review' by RF Weinberg and P. Hasalová. *Lithos*, 234, 100-101.
- 841 Cochelin, B., Lemirre, B., Denèle, Y., de Saint Blanquat, M. 2021. Strain partitioning within
842 bending orogens, new insights from the Variscan belt (Chiroulet-Lesponne domes,
843 Pyrenees). *Tectonics*, 40, e2020TC006386. <https://doi.org/10.1029/2020TC006386>
- 844 Collins, W.J., Huang, H.Q., Jiang, X.Y., 2016. Water-fluxed crustal melting produces
845 Cordilleran batholiths. *Geology* 44, 143–146.
- 846 Couzinié, S., Bouilhol, P., Laurent, O., Marko, L., Moyen, J. F., 2021. When zircon drowns:
847 Elusive geochronological record of water-fluxed orthogneiss melting in the Velay dome
848 (Massif Central, France). *Lithos*, 384, 105938.
- 849 D'Lemos, R.S., Brown, M., Strachan, R.A., 1992. The relationship between granite and shear
850 zones: magma generation, ascent and emplacement within a transpressional orogen.
851 *Journal of the Geological Society of London* 149, 487-490.
- 852 de Saint Blanquat, M., Horsman, E., Habert, G., Morgan, S., Vanderhaeghe, O., Law, R.,
853 Tikoff, B., 2011. Multiscale magmatic cyclicity, duration of pluton construction, and the
854 paradoxical relationship between tectonism and plutonism in continental arcs.
855 *Tectonophysics* 500, 20–33. doi:10.1016/j.tecto.2009.12.009.

- 856 Debon, F., Lemmet, M., 1999. Evolution of Mg/Fe ratios in late Variscan plutonic rocks from
857 the external crystalline massif of the Alps (France, Italy, Switzerland). *Journal of Petrology*
858 40, 1151–1185.
- 859 Debon, F., Cocherie, A., Ménot, R.-P., Vivier, G., Barféty, J.-C., 1994. Datation du plutonisme
860 magnésien varisque des massifs cristallins externes des Alpes: l'exemple du granite des Sept
861 Laux (massif de Belledonne, France). *Comptes Rendus de Academie des Sciences Paris Serie*
862 II, 318, 1497–1504.
- 863 Debon, F., Guerrot, C., Ménot, R.-P., Vivier, G., Cocherie, A., 1998. Late Variscan granites in
864 the Belledonne massif (French Western Alps): An Early Visean magnesian plutonism.
865 *Schweizerische Mineralogische und Petrographische Mitteilungen* 78, 67–85.
- 866 Dobmeier, C., 1996. Geodynamische Entwicklung dessüdwestlichen Aiguilles-Rouges Massivs
867 (West-alpen, Frankreich). *Mémoires de Géologie de Lausanne* 29, 1-198.
- 868 Dobmeier, C., 1998. Variscan P-T deformation paths from the southwestern Aiguilles Rouges
869 Massif (External massif, western Alps) and their implication for its tectonic evolution.
870 *Geologische Rundschau* 87, 107–123, doi:10.1007/s005310050193.
- 871 Dobmeier, C., von Raumer, JF., 1995. Significance of latest – Variscan and Alpine
872 deformation for the evolution of Montagne de Pormenaz (southwestern Aiguilles-Rouges
873 massif, western Alps). *Eclogae Geologicae Helvetiae* 88, 267–279.
- 874 Dobmeier, C., Pfeifer, HR., von Raumer, JF., 1999. The newly defined “Greenstone Unit” of
875 the Aiguilles-Rouges massif (western Alps); remnant of an early Palaeozoic oceanic island-
876 arc. *Schweizerische Mineralogische und Petrographische Mitteilungen* 79:263–276.

- 877 Dobmeier, C., Pfeifer, H. R., Von Raumer, J. F., 1999. The newly defined "Greenstone Unit" of
878 the Aiguilles Rouges massif (western Alps): remnant of an Early Palaeozoic oceanic island-
879 arc?. *Schweizerische Mineralogische und Petrographische Mitteilungen*, 79, 263-276.
- 880 Downes, H., Duthou, J. L., 1988. Isotopic and trace-element arguments for the lower-crustal
881 origin of Hercynian granitoids and Pre-Hercynian orthogneisses, Massif Central (France).
882 *Chemical Geology* 68, 291-308.
- 883 Downes, H., Shaw, A., Williamson, B. J., Thirlwall, M.F., 1997. Sr, Nd and Pb isotope
884 geochemistry of the Hercynian granodiorites and monzogranites, Massif Central, France.
885 *Chemical Geology* 136, 99-122.
- 886 Faure, M., Ferrière, J., 2022. Reconstructing the Variscan Terranes in the Alpine Basement:
887 Facts and Arguments for an Alpidic Orocline. *Geosciences*, 12(2), 65.
888 <https://doi.org/10.3390/geosciences12020065>
- 889 Fossen, H., Cavalcante, G.C.G., 2017. Shear zones—a review. *Earth Science Reviews* 171, 434–
890 455.
- 891 Franke, W., 2014, Topography of the Variscan orogen in Europe: Failed—not collapsed:
892 *International Journal of Earth Sciences*, v. 103, p. 1471–1499. doi:10.1007/s00531-014-1014-
893 9
- 894 Franke, W., Cocks, LRM., Torsvik, TH., 2017. The Palaeozoic Variscan oceans revisited.
895 *Gondwana Research*, 48, 257-284. <https://doi.org/10.1016/j.gr.2017.03.005>
- 896 Gapais, D., Potrel, A., Machado, N. 2005. Kinematics of long-lasting Paleoproterozoic
897 transpression within the Thompson Nickel Belt, Manitoba, Canada. *Tectonics* 24, TC3002.
898 doi:10.1029/2004TC001700

- 899 Genier, F., Bussy, F., Epard, J.L., Baumgartner, L., 2008. Water-Assisted Migmatization of
900 Metagraywackes in a Variscan Shear Zone, Aiguilles-Rouges Massif, Western Alps. *Lithos*
901 102, 575-597. <https://doi.org/10.1016/j.lithos.2007.07.024>.
- 902 Guerrot, C., Debon, F., 2000. U-Pb zircon dating of two contrasting Late Variscan plutonic
903 suites from the Pelvoux massif (French Western Alps). *Schweizerische Mineralogische und*
904 *Petrographische Mitteilungen* 80, 249–256.
- 905 Guillot, St., di Paola, S., Ménot, R.-P., Ledru, P., Spalla, M.I., Gosso, G., and Schwartz, St.,
906 2009, Suture zones and importance of strike-slip faulting for Variscan geodynamic
907 reconstructions of the External Crystalline Massifs of the western Alps: *Bulletin de la Société*
908 *Géologique de France* 180, 483–500, doi:10.2113/gssgfbull.180.6.483.
- 909 Guillot, F., Averbuch, O., Dubois, M., Durand, C., Lanari, P., Gauthier, A., 2020. Zircon age of
910 vaugnerite intrusives from the Central and Southern Vosges crystalline massif (E France):
911 contribution to the geodynamics of the European Variscan belt. *Bulletin de la Société*
912 *Géologique de France* 191, 26. <https://doi.org/10.1051/bsgf/2020027>
- 913 Hurai, V., Paquette, J.L., Huraiová, M., Konečný, P., 2010. Age of deep crustal magmatic
914 chambers in the intra-Carpathian back-arc basin inferred from LA-ICPMS U-Th-Pb dating of
915 zircon and monazite from igneous xenoliths in alkali basalts. *Journal of Volcanology and*
916 *Geothermal Research* 198, 275-287.
- 917 Jackson, S.E., Pearson, N.J., Griffin, W.L., Belousova, E.A., 2004. The application of laser
918 ablation-inductively coupled plasma-mass spectrometry to in situ U–Pb zircon
919 geochronology. *Chemical Geology* 211, 47-69.

- 920 Jacob, J.-B., Moyen, J.-F., Fiannacca, P., Laurent, O., Bachmann, O., Janousek, V., Farina, F.,
921 Villaros, A., 2021. Crustal melting vs. fractionation of basaltic magmas: part 2, Attempting to
922 quantify mantle and crustal contributions in granitoids. *Lithos* 402-403, 106292.
- 923 Joye, JB., 1989. L'évolution pression-température-déformation dans le massif des Aiguilles
924 Rouges, massif externe alpin, (PhD thesis). Fribourg, Switzerland, Université de Fribourg.
925 78p.
- 926 Kelsey, D.E., Clark, C., Hand, M., 2008. Thermobarometric modelling of zircon and monazite
927 growth in melt-bearing systems: examples using model metapelitic and metapsammitic
928 granulites. *Journal of Metamorphic Geology* 26, 199–212.
- 929 Krummenacher, D., 1959. Le cristallin de la région de Fully (Valais). *Schweizerische*
930 *Mineralogische und Petrographische Mitteilungen* 39, 151-266.
- 931 Laurent, O., Couzinié, S., Zeh, A., Vanderhaeghe, O., Moyen, J.F., Villaros, A., Gardien, V.,
932 Chelle-Michou, C., 2017. Protracted, coeval crust and mantle melting during Variscan late
933 orogenic evolution: U–Pb dating in the eastern French Massif Central. *International Journal*
934 *of Earth Sciences* 106, 421-451.
- 935 Li, X.H., Faure, M., Lin, W., 2014. From crustal anatexis to mantle melting in the Variscan
936 orogen of Corsica (France): SIMS U–Pb zircon age constraints. *Tectonophysics* 634, 19–30
- 937 Liégeois, JP., Duchesne, JC., 1981. The Lac Cornu Retrograded Eclogites (Aiguilles Rouges
938 Massif, Western Alps France): Evidence of Crustal Origin and Metasomatic Alteration. *Lithos*
939 14, 35-48.
- 940 Linnemann, U., Ouzegane, K., Drareni, A., Hofmann, M., Becker, S., Gärtner, A., Sagawe, A.,
941 2011. Sands of West Gondwana: an archive of secular magmatism and plate interactions—a

- 942 case study from the Cambro-Ordovician section of the Tassili Ouan Ahaggar (Algerian
943 Sahara) using U–Pb LA-ICP-MS detrital zircon ages. *Lithos* 123, 188–203.
- 944 Lopez-Sanchez, M. A., Aleinikoff, J. N., Marcos, A., Martínez, F. J., Llana-Fúnez, S., 2016. An
945 example of low-Th/U zircon overgrowths of magmatic origin in a late orogenic Variscan
946 intrusion: the San Ciprián massif (NW Spain). *Journal of the Geological Society*, 173(2), 282-
947 291.
- 948 Lotout, C., Pitra, P., Poujol, M., Van Den Driessche, J., 2017. Ordovician magmatism in the
949 Lévézou massif (French Massif Central): tectonic and geodynamic implications. *International*
950 *Journal of Earth Sciences* 106 (2), 501–515. <https://doi.org/10.1007/s00531-016-1387-z>.
- 951 Lox, A., Bellière, J., 1993. Le Silésien (Carbonifère Supérieur) de Pormenaz (Massif des
952 Aiguilles-Rouges): lithologie et tectonique. *Eclogae Geologicae Helvetiae* 86, 769–783.
- 953 Ludwig, KR., 2001. User manual for Isoplot/Ex rev. 2.49. A geochronological toolkit for
954 Microsoft Excel. Berkeley Geochronology Center Special Publication 1a, 1–56.
- 955 Maierova, P., Schulmann, K., Gerya, T., 2018. Relamination styles in collisional orogens.
956 *Tectonics* 37, 224–250.
- 957 Maierova, P., Schulmann, K., Stípska, P., Gerya, T., Lexa, O., 2021. Trans-litospheric diapirism
958 explains the presence of ultra-high pressure rock in the European Variscides.
959 *Communications Earth and Environment* 2, 56. [https://doi.org/10.1038/s43247-021-00122-](https://doi.org/10.1038/s43247-021-00122-w)
960 *w*.
- 961 Marshall, D., Kirschner, D., Bussy, F., 1997. A variscan pressure–temperature–time path for
962 the N–E Mont Blanc massif. *Contribution to Mineralogy and Petrology* 126, 416–428

- 963 Martinez-Catalán, J. R., Schulmann, K., Ghienne, J. F., 2021. The Mid-Variscan Allochthon:
964 Keys from correlation, partial retrodeformation and plate-tectonic reconstruction to unlock
965 the geometry of a non-cylindrical belt. *Earth-Science Reviews*, 220, 103700.
- 966 Melleton, J., Cocherie, A., Faure, M., Rossi, P. 2010. Precambrian protoliths and Early
967 Paleozoic magmatism in the French Massif Central: U–Pb data and the North Gondwana
968 connection in the west European Variscan belt. *Gondwana Research*, 17, 13–25.
- 969 Mintrone, M., Galli, A., Laurent, O., Chelle-Michou, C., Schmidt, M.W., 2020. Quantifying
970 frozen melt in crustal rocks: a new melt-o-meter based on zircon rim volumes. *Chemical
971 Geology* 551, 119755.
- 972 Müller, W., Shelley, M., Miller, P., Broude, S., 2009. Initial performance metrics of a new
973 custom-designed ArF excimer LA-ICPMS system coupled to a two-volume laser-ablation cell.
974 *Journal of Analytical Atomic Spectrometry.*, 24:209-214.
- 975 Neiva, A.M.R., Williams, I.S., Lima, S.M., Teixeira, R.J.S., 2012. U–Pb and ³⁹Ar/⁴⁰Ar data
976 constraining the ages of the source, emplacement and recrystallization/cooling events from
977 late- to post-D3 Variscan granites of the Gouveia area, central Portugal. *Lithos* 153, 72–83.
- 978 Neves, S. P., Vauchez, A., Archanjo, C. J., 1996. Shear zone-controlled magma emplacement
979 or magma-assisted nucleation of shear zones? Insights from northeast Brazil.
980 *Tectonophysics*, 262(1-4), 349-364.
- 981 Oriolo, S., Wemmer, K., Oyhantçabal, P., Fossen, H., Schulz, B., Siegesmund, S., 2018.
982 *Geochronology of shear zones—A review. Earth Science Reviews* 185, 665–683.
- 983 Paquette, J.L., Tiepolo, M., 2007. High resolution (5 μm) U-Th-Pb isotopes dating of monazite
984 with excimer laser ablation (ELA)-ICPMS. *Chemical Geology*, 240, 222-237.

- 985 Paquette, J.L., Menot, R.P., Peucat, J.J., 1989. REE, Sm-Nd and U-Pb zircon study of eclogites
986 from the Alpine External Massifs (Western Alps): evidence for crustal contamination. *Earth
987 and Planetary Sciences Letters* 96, 181-198.
- 988 Paquette, J. L., Ménot, R. P., Pin, C., Orsini, J. B., 2003. Episodic and short-lived granitic
989 pulses in a post-collisional setting: evidence from precise U–Pb zircon dating through a
990 crustal cross-section in Corsica. *Chemical Geology*, 198(1-2), 1-20.
- 991 Paquette, J.L., Piro, J.L., Devidal, J.L., Bosse, V., Didier, A., 2014. Sensitivity enhancement in LA-
992 ICP-MS by N₂ addition to carrier gas: application to radiometric dating of U–Th-bearing
993 minerals. *Agilent ICP-MS Journal* 58, 4–5.
- 994 Passchier, C.W., Trouw, R.A.J., 2005. *Microtectonics*. Springer, Berlin, p. 289.
- 995 Pawley, M.J., Collins, W.J., 2002. The development of contrasting structures during the
996 cooling and crystallisation of a syn-kinematic pluton. *Journal of Structural Geology* 24, 469–
997 483.
- 998 Pilloud, C., 1991. Structure de déformation alpines dans le synclinal de Permo-Carbonifère
999 de Salvan-Dorenaz, (massif des Aiguilles Rouges, Valais). *Mémoires de Géologie de Lausanne*
1000 9, 1-101.
- 1001 Pin, C., Duthou, J. L., 1990. Sources of Hercynian granitoids from the French Massif Central:
1002 Inferences from Nd isotopies and consequences for crustal evolution. *Chemical Geology* 83,
1003 281-96.
- 1004 Rodríguez, C., Pereira, M. F., Castro, A., Gutiérrez-Alonso, G., Fernández, C., 2022. Variscan
1005 intracrustal recycling by melting of Carboniferous arc-like igneous protoliths (Évora Massif,
1006 Iberian Variscan belt). *Bulletin*, 134(5-6), 1549-1570.

- 1007 Rolland, Y., Cox, S., Boullier, AM., Pennacchioni, G., Mancktelow, N., 2003. Rare earth and
1008 trace element mobility in mid-crustal shear zones: Insights from the Mont Blanc Massif
1009 (western Alps), *Earth and Planetary Sciences Letters* 214, 203–219.
- 1010 Rossi, M., Rolland, Y., Vidal, O., Cox, S., 2005. Geochemical variations and element transfer
1011 during shear zone development and related episyenites at middle crust depths: Insights from
1012 the Mont-Blanc granite (French-Italian Alps). In D. Brunh and L. Burlini (Eds.), *High Strain
1013 Zones: Structure and Physical Properties*, Geological Society, London, Special Publication,
1014 245, 373-396.
- 1015 Rossi, P., Oggiano, G., Cocherie, A., 2009. A restored section of the “southern Variscan
1016 realm” across the Corsica–Sardinia microcontinent. *Mécanique de l’orogénie varisque : Une
1017 vision moderne de la recherche dans le domaine de l’orogénie. Comptes Rendus Geoscience*,
1018 341, 224–238. <https://doi.org/10.1016/j.crte.2008.12.005>
- 1019 Rubatto, D., Schaltegger, U., Lombardo, B., Colombo, F., Compagnoni, R., 2001. Complex
1020 Paleozoic magmatic and metamorphic evolution in the Argentera Massif (Western Alps)
1021 resolved with U-Pb dating. *Schweizerische Mineralogische und Petrographische
1022 Mitteilungen*, 81, 213–228.
- 1023 Sawyer, E. W., 2010. Migmatites formed by water-fluxed partial melting of a
1024 leucogranodiorite protolith: Microstructures in the residual rocks and source of the fluid.
1025 *Lithos*, 116(3-4), 273-286.
- 1026 Sawyer, E. W., Cesare, B., Brown, M. 2011. When the continental crust melts. *Elements* 7,
1027 229–234

- 1028 Schaltegger, U., Corfu, F. 1992, The age and source for late Hercynian magmatism in the
1029 Central Alps: Evidence from precise U–Pb ages and initial Hf isotopes. *Contributions to*
1030 *Mineralogy and Petrology* 111, 329–344.
- 1031 Schulz, B., von Raumer, JF., 1993. Syndeformational Uplift of Variscan High-pressure Rocks
1032 (Col de Bérard, Aiguilles Rouges Massif, Western Alps). *Zeitschrift der Deutschen*
1033 *Geologischen Gesellschaft* 144, 104-120.
- 1034 Schulz, B., von Raumer, J., 2011. Discovery of Ordovician–Silurian metamorphic monazite in
1035 garnet metapelites of the Alpine External Aiguilles Rouges Massif. *Swiss Journal of*
1036 *Geosciences* 104:67–79. doi:10.1007/s00015-010-0048-7.
- 1037 Simonetti, M., Carosi, R., Montomoli, C., Langone, A., D’Addario, E., & Mammoliti, E., 2018.
1038 Kinematic and geochronological constraints on shear deformation in the Ferriere-Mollières
1039 shear zone (Argentera-Mercantour Massif, Western Alps): Implications for the evolution of
1040 the Southern European Variscan Belt. *International Journal of Earth Sciences*, 107(6), 2163-
1041 2189.
- 1042 Simonetti, M., Carosi, R., Montomoli, C., Cottle, JM., Law, RD., 2020. Transpressive
1043 Deformation in the Southern European Variscan Belt: New Insights From the Aiguilles Rouges
1044 Massif (Western Alps). *Tectonics*, 39. <https://doi.org/10.1029/2020TC006153>
- 1045 Simonetti, M., Carosi, R., Montomoli, C., Law, R. D., Cottle, J. M., 2021. Unravelling the
1046 development of regional-scale shear zones by a multidisciplinary approach: The case study of
1047 the Ferriere-Mollières Shear Zone (Argentera Massif, Western Alps). *Journal of Structural*
1048 *Geology*, 149, 104399.

- 1049 Tabaud, A-S., Whitechurch, H., Rossi, P., Schulmann, K., Guerrot, C., Cocherie, A., 2014.
1050 Devonian-Permian magmatic pulses in the northern Vosges Mountains (NE France): result of
1051 continuous subduction of the Rhenohercynian Ocean and Avalonian passive margin.
1052 Geological Society, London, Special Publications 405, 197–223.
- 1053 Tabaud, A-S., Janouzek, V., Skrzypek, E., Schulmann, K., Rossi, P., Whitechurch, H., Guerrot,
1054 C., Paquette, JL., 2015. Chronology, petrogenesis and heat sources for successive
1055 Carboniferous magmatic events in the Southern-Central Variscan Vosges Mts (NE France).
1056 Journal of the Geological Society, London 172: 87–102.
- 1057 Teipel, U., Eichhorn, R., Loth, G., Rohrmüller, J., Höll, R., Kennedy, A., 2004. U–Pb SHRIMP
1058 and Nd isotopic data from the western Bohemian Massif (Bayerischer Wald, Germany).
1059 International Journal of Earth Sciences 93, 782–801.
- 1060 Tikoff, B., Teyssier, C., 1994. Strain modelling of displacement-field partitioning in
1061 transpressional orogens. Journal of Structural Geology 16, 1575 – 1588.
- 1062 Tommasi, A., Vauchez, A., Fernandes, L.A.D., Porcher, C.C., 1994. Magma assisted strain
1063 localization in an orogen-parallel transcurrent shear zone of southern Brazil. Tectonics 13,
1064 421–437.
- 1065 Turpin, L., Cuney, M., Friedrich, M., Bouchez, J-L., Aubertin, M., 1990. Meta-igneous origin of
1066 Hercynian peraluminous granites in N. W. French Massif Central: Implications for crustal
1067 history reconstructions. Contributions to Mineralogy and Petrology 104, 163-72.
- 1068 Vanardois, J., Roger, F., Trap, P., Goncalves, P., Lanari, P., Paquette, JL., Marquer, D.,
1069 Cagnard, F., Le Bayon, B., Melleton, J., Barou, F., 2022. Exhumation of deep continental crust

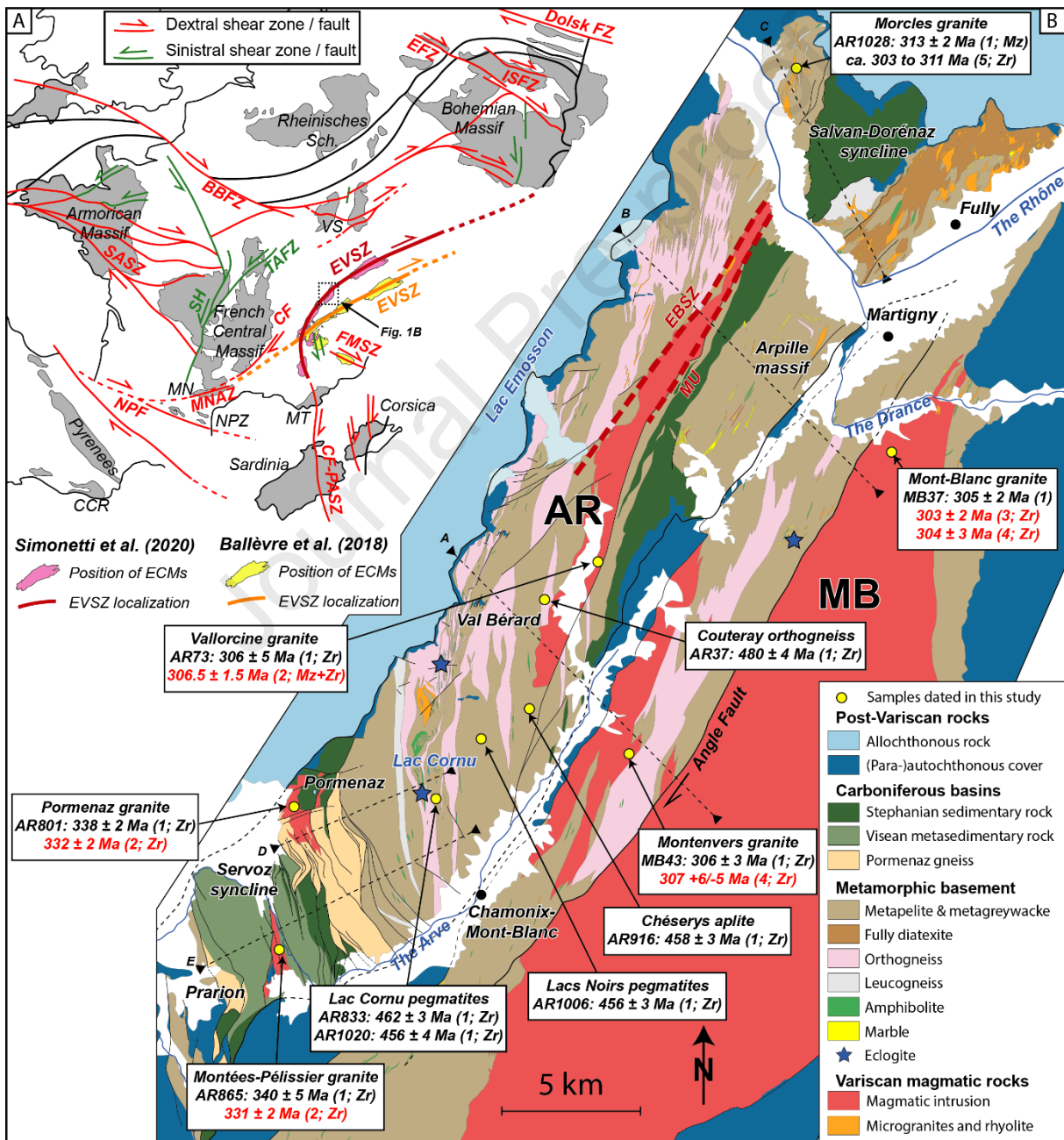
- 1070 in a transpressive regime: the example of Variscan eclogites from Aiguilles-Rouges Massif
1071 (Western Alps). *Journal of Metamorphic Geology*. <https://doi.org/10.1111/jmg.12659>
- 1072 Vanderhaeghe, O., Laurent, O., Gardien, V., Moyen, J.F., Gébelin, A., Chelle-Michou, C.,
1073 Couzinié, S., Villaros, A., Bellanger, M., 2020. Flow of partially molten crust controlling
1074 construction, growth and collapse of the Variscan orogenic belt: the geologic record of the
1075 French Massif Central. *Bulletin de la Société géologique de France*, 191,
1076 doi.org/10.1051/bsgf/2020013.
- 1077 Villaseca, C., Orejana, D., Belousova, E.A., 2012. Recycled metagneous crustal sources for S-
1078 and I-type Variscan granitoids from the Spanish Central System batholith: Constraints from
1079 Hf isotope zircon composition. *Lithos* 153, 84–93.
- 1080 Vitel, G., 1965. Etude pétrographique du tunnel du Mont-Blanc (partie française) et
1081 recherches géologiques complémentaires dans le massif Mont-Blanc - Aiguilles-Rouges. PhD
1082 Thesis, University of Grenoble, France.
- 1083 von Raumer, J.F., 1984. The external massifs, relics of Variscan basement in the Alps.
1084 *Geologische Rundschau* 73:1–31.
- 1085 von Raumer, J.F., Bussy, F., 2004. Mont-Blanc and Aiguilles-Rouges: Geology of their
1086 polymetamorphic basement (External massifs, France-Switzerland). *Mémoires de Géologie*
1087 *de Lausanne* 42, 1–203.
- 1088 Von Raumer, J.F., Schwander, H.W., 1985. Garnet evolution in pre-Variscan pelitic rocks from
1089 the Lac Emosson area, Aiguilles Rouges Massif, Western Alps. *Journal of Metamorphic*
1090 *Geology* 3, 467–479.

- 1091 von Raumer, J.F., Bussy, F., Sharp, Z., 1996. Lac Cornu revisited: The evolution from lower to
1092 upper crust (Aiguilles-Rouges Massif, western Alps). *Schweizerische Mineralogische und*
1093 *Petrographische Mitteilungen* 76:120–121.
- 1094 Watson, E.B., 1996. Dissolution, growth and survival of zircons during crustal fusion: kinetic
1095 principals, geological models and implications for isotopic inheritance. *Transactions of the*
1096 *Royal Society of Edinburgh* 87, 43–56.
- 1097 Watson, E.B., Harrison, T.M., 1983. Zircon saturation revisited: temperature and composition
1098 effects in a variety of crustal magma types. *Earth and Planetary Sciences Letters* 64, 295–
1099 304.
- 1100 Weinberg, R. F., Hasalová, P., 2015. Water-fluxed melting of the continental crust: A review.
1101 *Lithos* 212, 158-188.
- 1102 White, R. W., Pomroy, N. E., Powell, R., 2005. An in situ metatexite–diatexite transition in
1103 upper amphibolite facies rocks from Broken Hill, Australia. *Journal of Metamorphic Geology*,
1104 23(7), 579-602.
- 1105 Xu, Z., Wang, Q., Cai, Z., Dong, H., Li, H., Chen, X., Duan, X., Cao, H., Li, J., Burg, JP. 2015.
1106 Kinematics of the Tengchong Terrane in SE Tibet from the late Eocene to early Miocene:
1107 insights from coeval mid-crustal detachments and strike-slip shear zones. *Tectonophysics*
1108 665, 127-148. doi.org/10.1016/j.tecto.2015.09.033.
- 1109 Yakymchuk, C., Brown, M., 2014. Behaviour of zircon and monazite during crustal melting.
1110 *Journal of the Geological Society, London* 171, 465–479.

1111 Yin, A., Taylor, MH. 2011. Mechanics of V-shaped conjugate strike-slip faults and the
 1112 corresponding continuum mode of continental deformation. Geological Society of America
 1113 Bulletin, 123, 1798–1821. doi.org/10.1130/B30159.1

1114

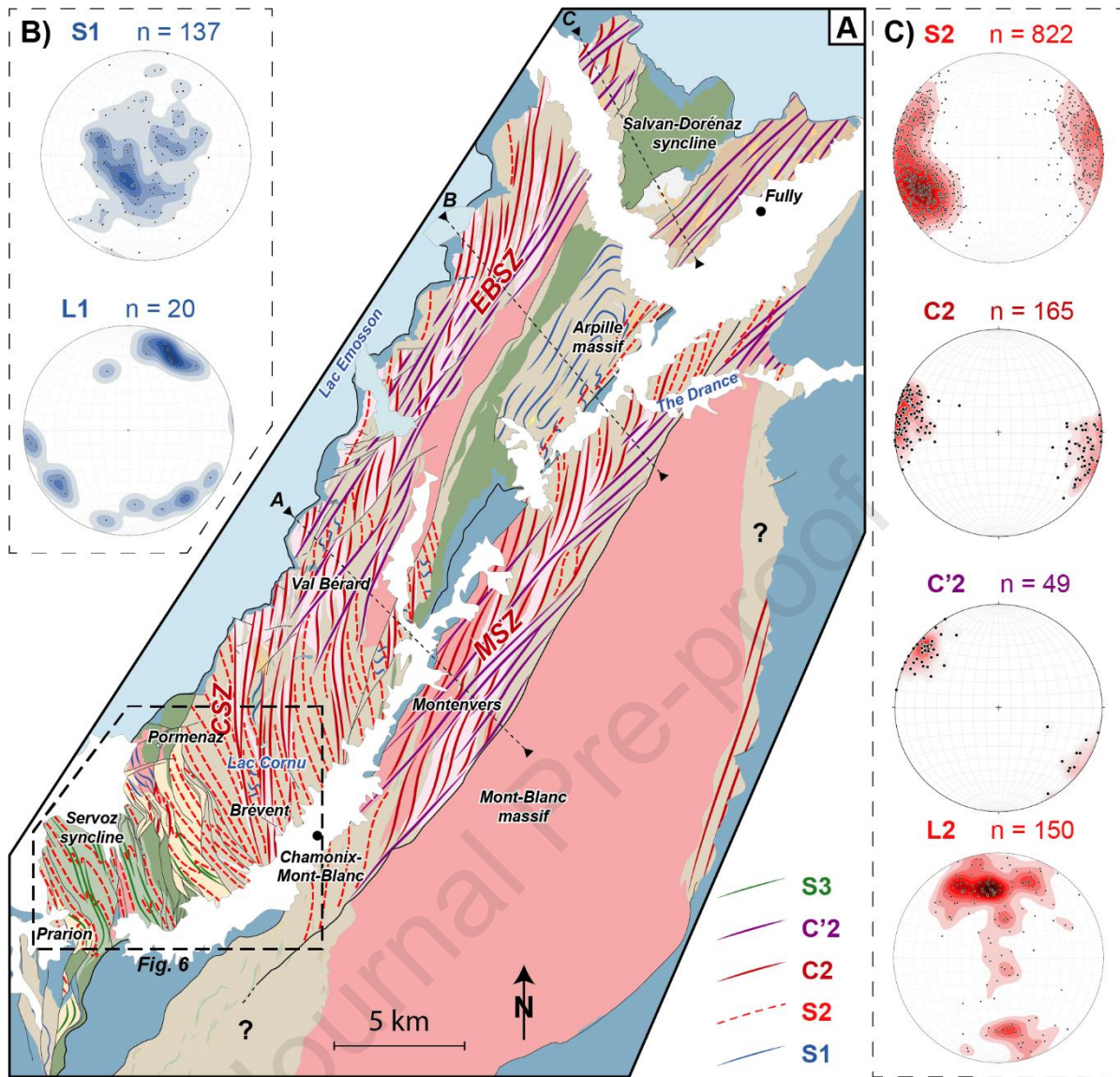
1115 **Figure captions**



1116

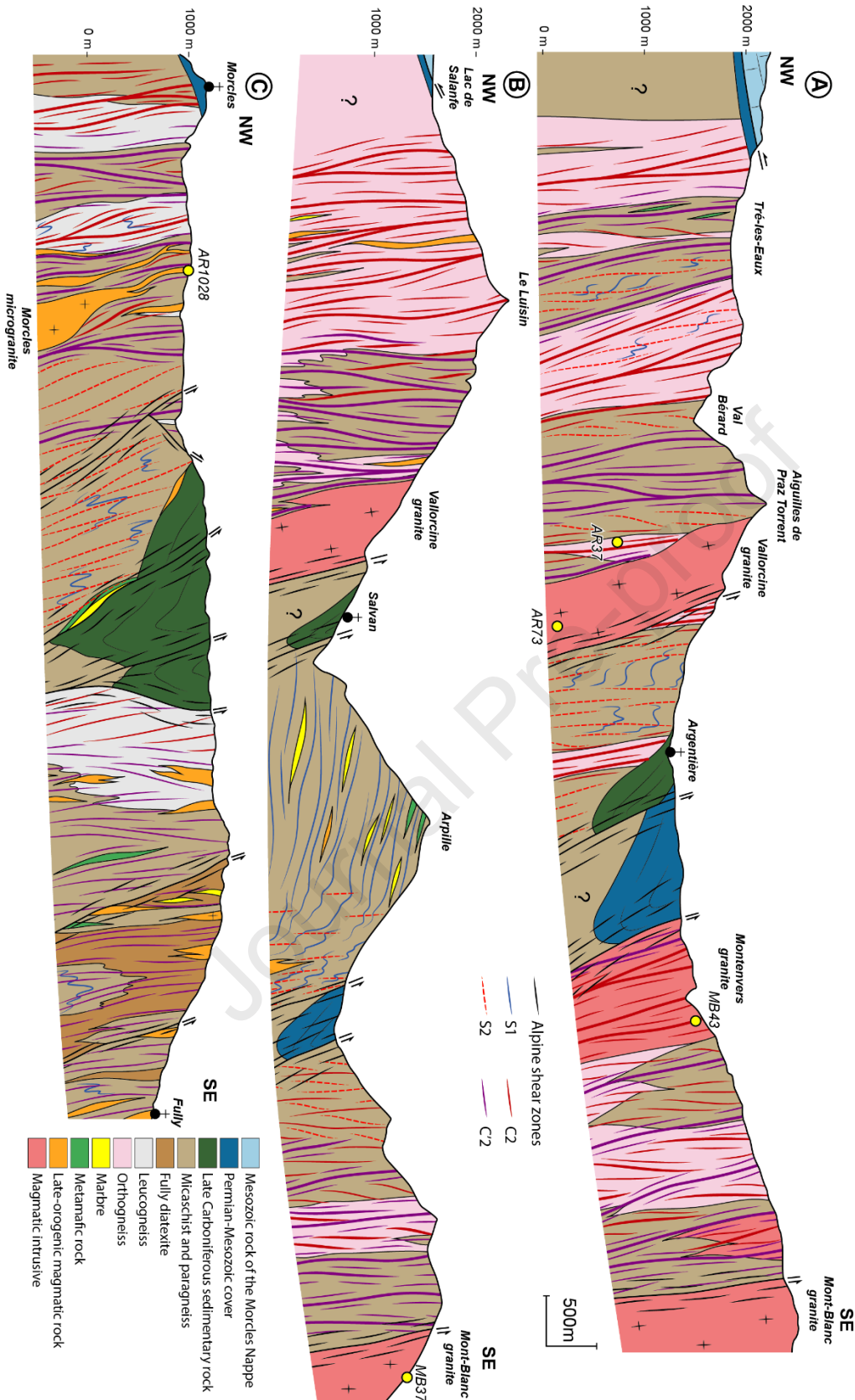
1117 **Fig. 1:** (A) Paleogeographic reconstitution of the European Variscan Belt at the end of the
1118 Variscan orogeny modified from Franke et al. (2017). Sardinia and Corsica have the same
1119 position as the one used in Simonetti et al. (2020). Models of the EVSZ are after Simonetti et
1120 al. (2020) and Ballèvre et al. (2018). The position of ECMs is after Bellahsen et al. (2014) in the
1121 Ballèvre et al. (2018) model. *BBFZ*: Bristol Bray Fault Zone; *CCR*: Catalan Coastal Ranges; *CF*:
1122 Cévennes Fault; *EFZ*: Elbe Fault Zone; *EVSZ*: East Variscan Shear Zone; *FMSZ*: Ferrière-Mollière
1123 Shear Zone; *CF-PASZ*: Cavalaire Fault - Posada-Asinara Shear Zone; *ISFZ*: Intra-Sudetic Fault
1124 Zone; *MN*: Montagne Noire; *MNAZ*: Montagne Noire Axial Zone; *NPF*: North Pyrenean Fault;
1125 *NPZ*: North Pyrenean Zone; *SASZ*: South Armorican Shear Zone; *SH*: Sillon Houiller fault; *TAFZ*:
1126 Taure-Aigueperse Fault Zone; *VS*: Vosges-Schwarzwald. (B) Geological map of the Aiguilles-
1127 Rouges (AR) and the Mont-Blanc (MB) Massifs with geochronological results and sample
1128 locations. *EBSZ*: Emosson-Bérard shear zone; *MU*: Miéville ultramylonite. Synthesis of
1129 Variscan ages obtained by ID-TIMS (red) and LA-ICPMS (black) U-Th-Pb method on zircon (Zr)
1130 and monazite (Mz) after (1) this study, (2) Bussy et al. (2000), (3) Bussy and von Raumer (1993),
1131 (4) Bussy and von Raumer (1994), (5) Bussien et al. (2017). Structure sections A, B, C, D and E
1132 are to those in Figures 3 and 7.

1133



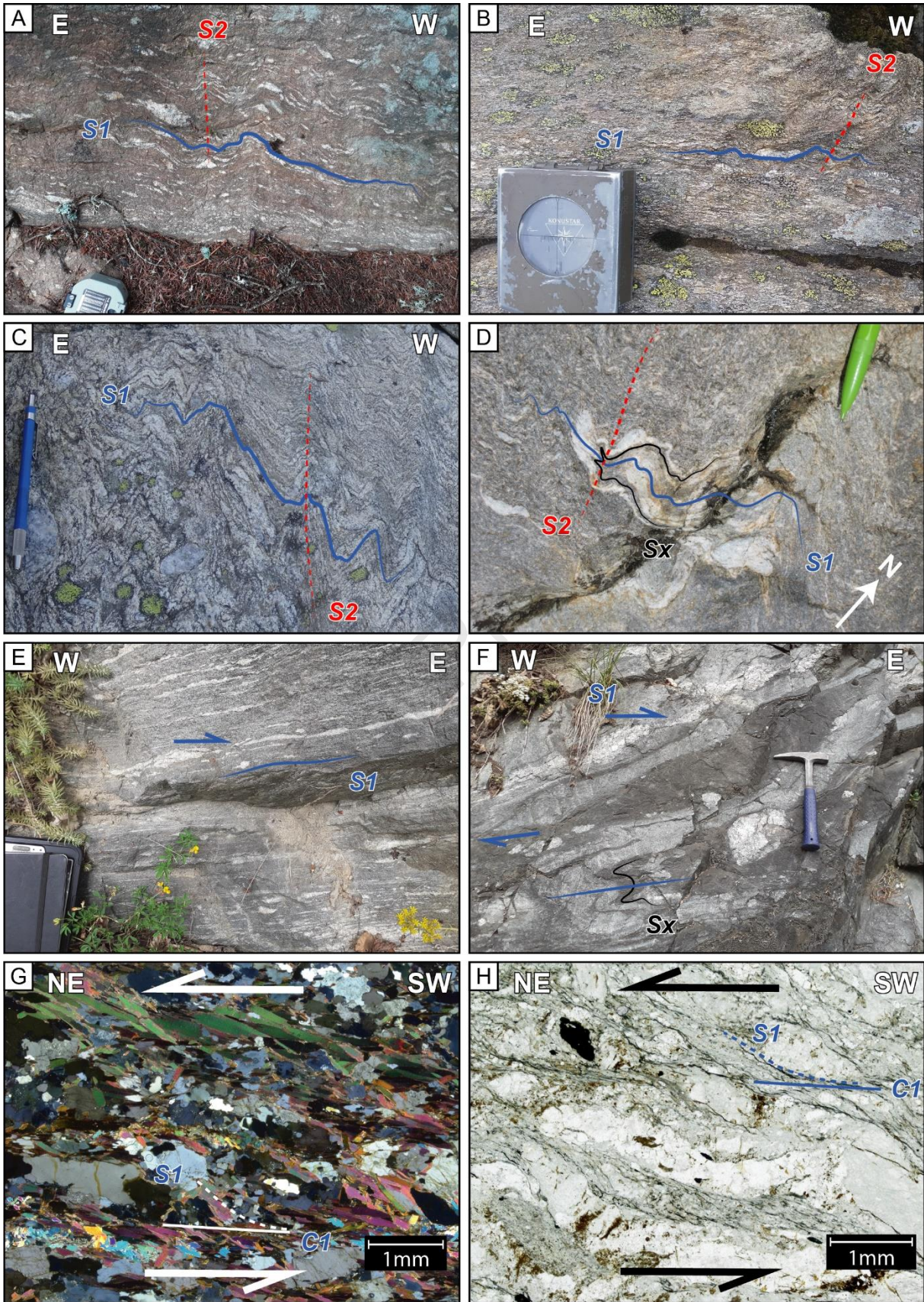
1134

1135 **Fig. 2:** (A) Synthetic map showing the simplified foliation trajectories of D1, D2 and D3
 1136 deformation. Lithological legend is the same as in Figure 1B. The area corresponding to Figure
 1137 6 is indicated. CSZ: Cornu Shear Zone; EBSZ: Emosson-Bérard Shear Zone; MSZ: Montenvers
 1138 Shear Zone. (B and C) Stereograms of poles to planar fabrics and mineral lineation for D1 and
 1139 D2 deformation are Wulff lower-hemisphere projections.



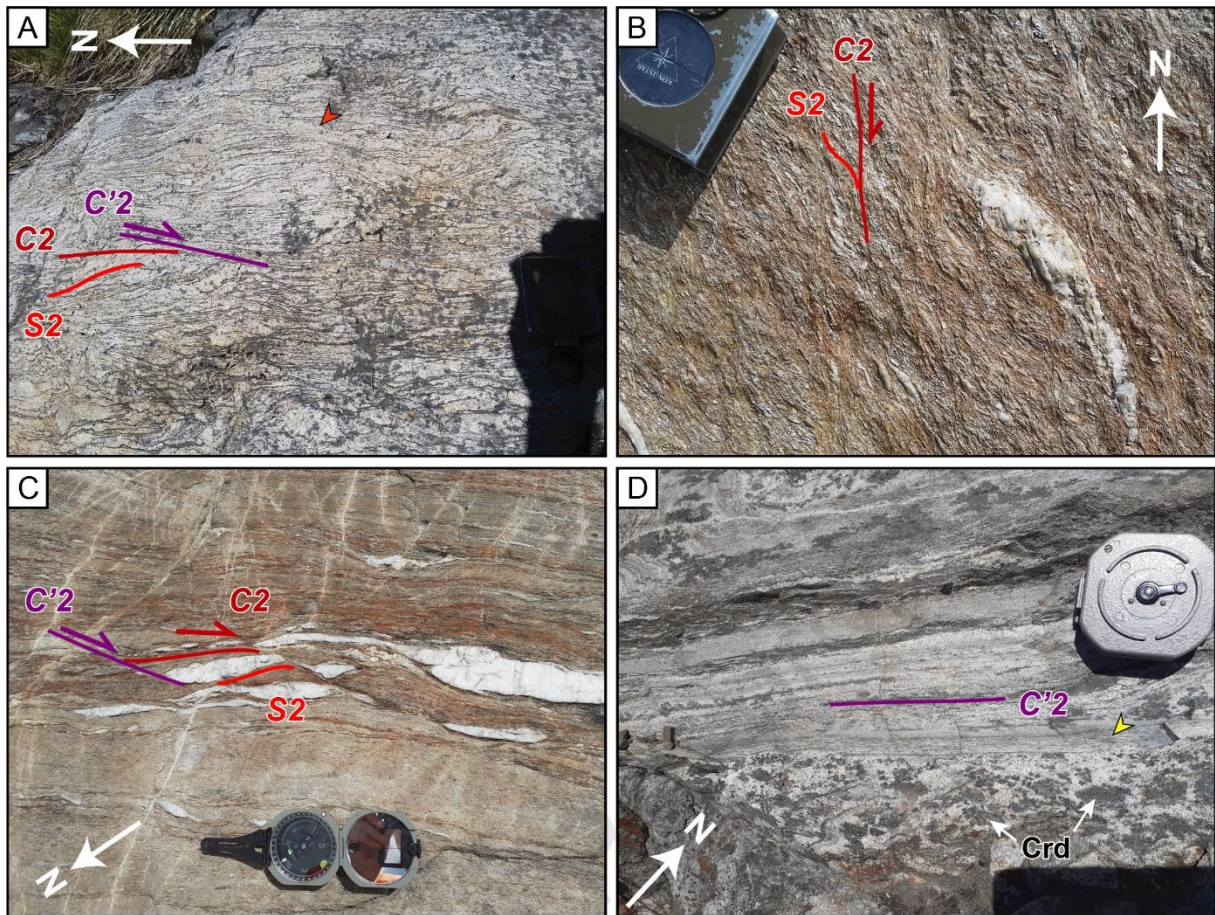
1140

1141 **Fig. 3:** E-W Structure sections through the Aiguilles-Rouges and the Mont-Blanc Massifs (see
 1142 location of sections on Figures 1 and 2). Same structures symbols as in Figure 2.



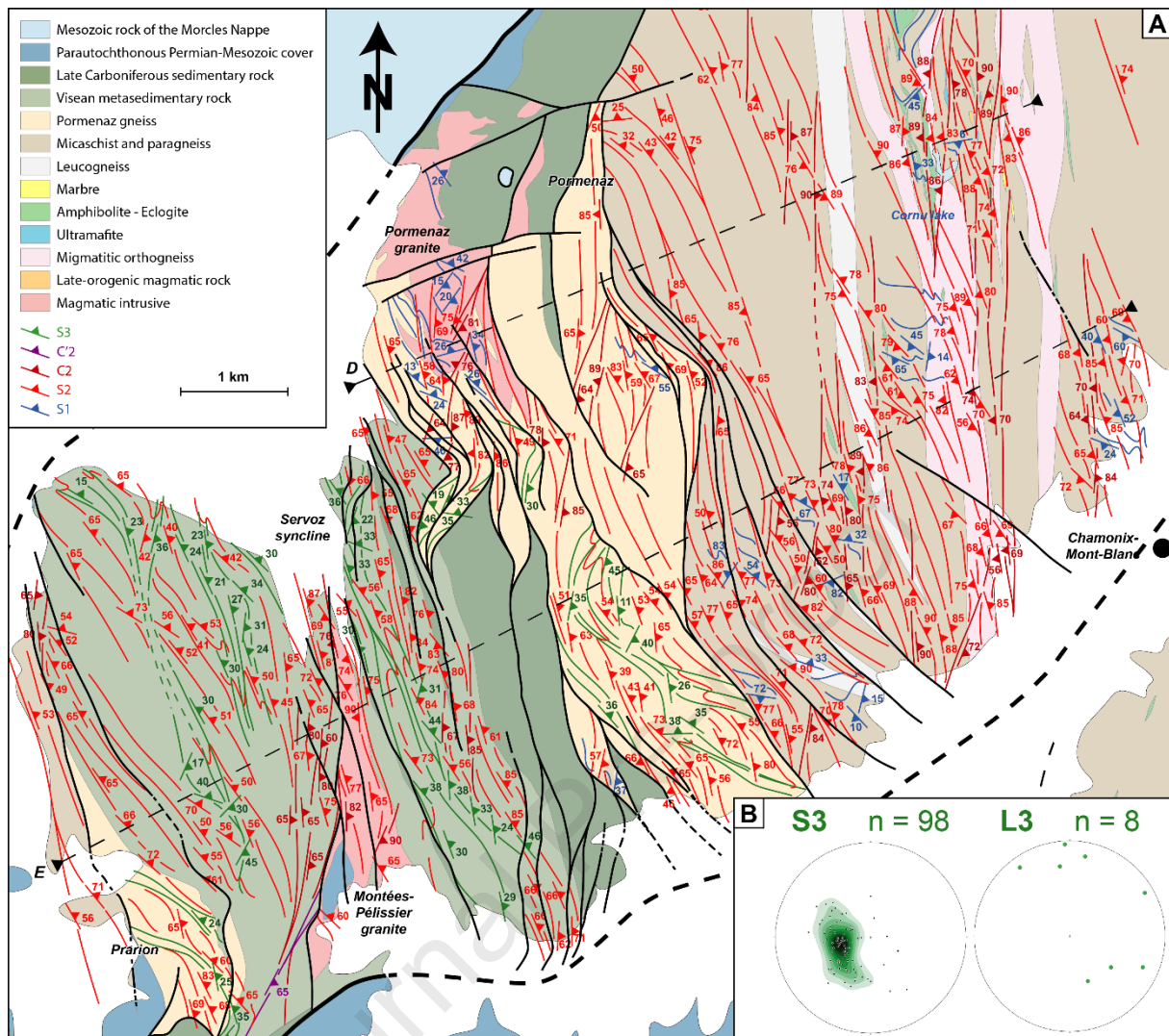
1144 **Fig. 4:** D1 deformation and D1/D2 relationships. S1 foliation and weak S2 schistosity in the
1145 Arpille massif (A; N46.110779; E7.039935), near the Brévent location (B; N45.941226;
1146 E6.842971) and in the Lac Cornu area (C; N45.956048; E6.853897). (D) D1/D2 fold
1147 interference: an F1 fold deforming an Sx foliation, the S1 foliation is subsequently deformed
1148 by F2 folds with an associated S2 schistosity, Val Bérard area (N46.004630; E6.872713). (E and
1149 F) Top-to-the-NE kinematics indicated by asymmetric boudinage/structures in Prarion
1150 metabasites (N45.865415; E6.734047). (G) Top-to-the-NE kinematics indicated by sheared
1151 biotite mica-fish, Arpille massif (N46.110362; E7.040006). (H) Top-to-the-NE C-S structures in
1152 a low-grade Pormenaz gneiss (N45.941793; E6.782782).

1153



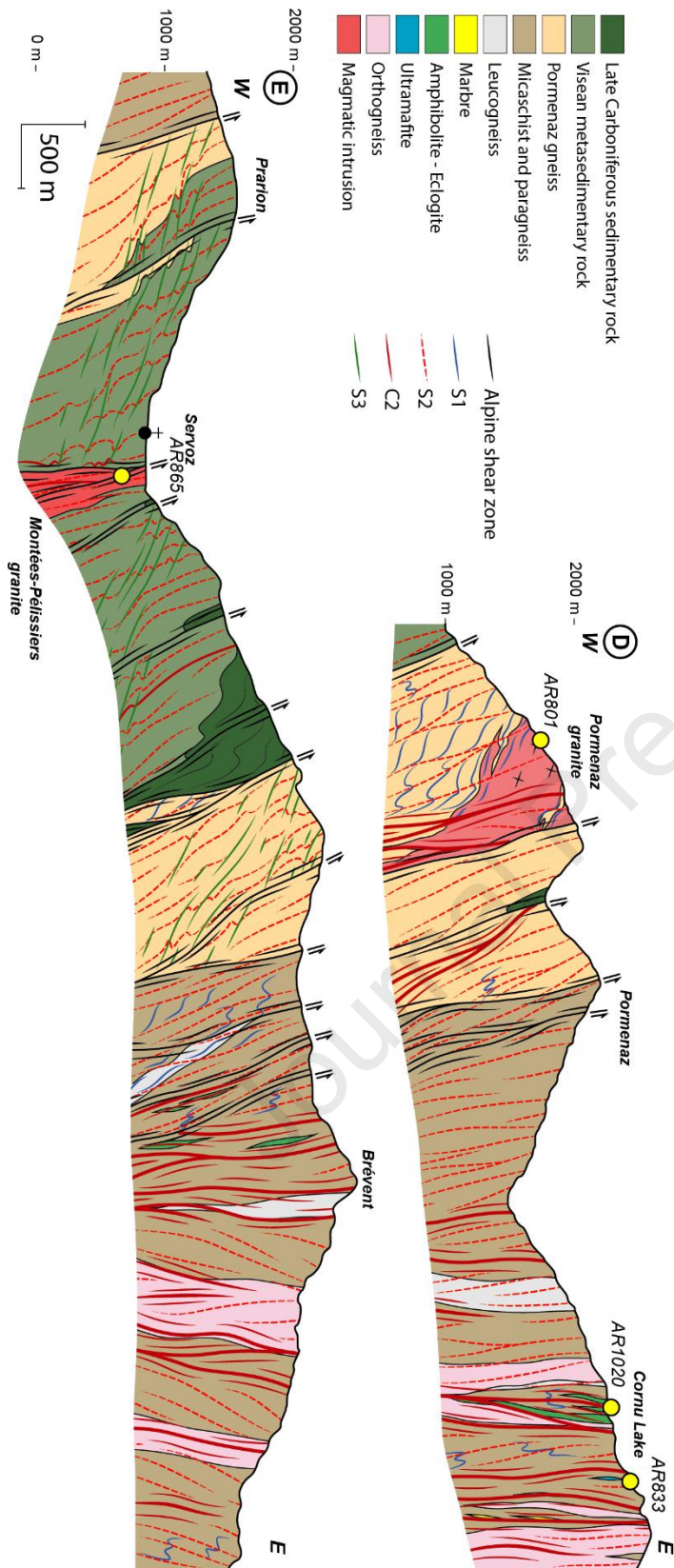
1154

1155 **Fig. 5:** D2 deformation. S2-C2-C'2 structures in the Lac Cornu area (A) (N46.066231;
 1156 E6.916211) and near Chamonix-Mont-Blanc (B) (N45.927587; E6.825600). Red arrow indicates
 1157 melt injection in a C'2 shear band. (C) S2-C2-C'2 structures in the Lac Emosson area
 1158 (N46.067197; E6.923349). (D) Cordierite-bearing migmatite with cordierite clots (Crd)
 1159 oriented parallel with C'2 planes and centimeter-sized ultramylonitic C'2 shear bands (yellow
 1160 arrow) (N46.123427; E7.078374).



1161

1162 **Fig. 6:** (A) Detailed map of the D1-D2-D3 foliations and their trajectories in the southwestern
 1163 part of the Aiguilles-Rouges Massif. (B) Stereograms of poles of planar fabrics and lineations
 1164 of D3 deformation are Wulff lower-hemisphere projections. Location of structure sections D
 1165 and E is indicated.

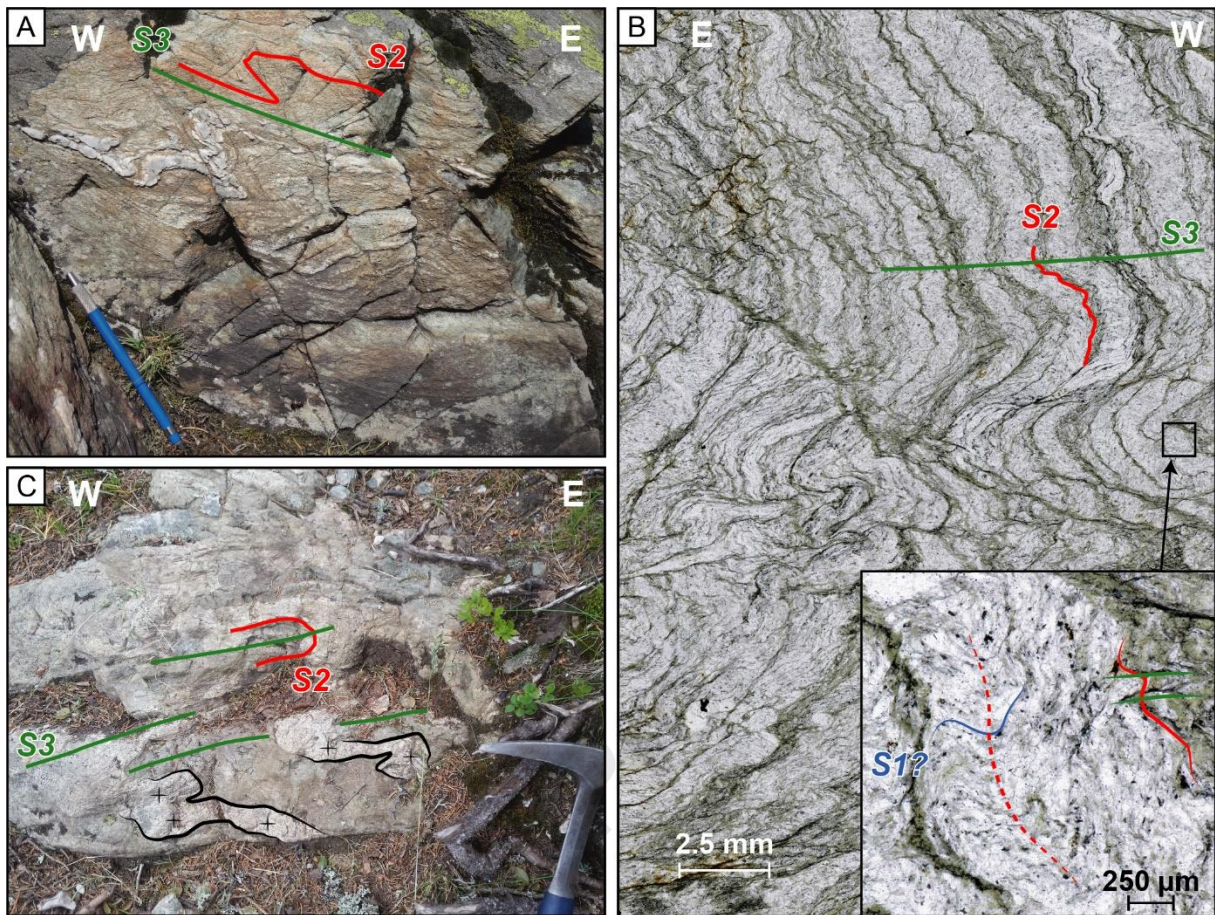


1166

1167 **Fig. 7:** E-W structure sections at the southwestern extremity of the Aiguilles-Rouges Massif.

1168 (D) In the Pormenaz area and (E) through the Servoz syncline. Location on Figure 6.

1169



1170

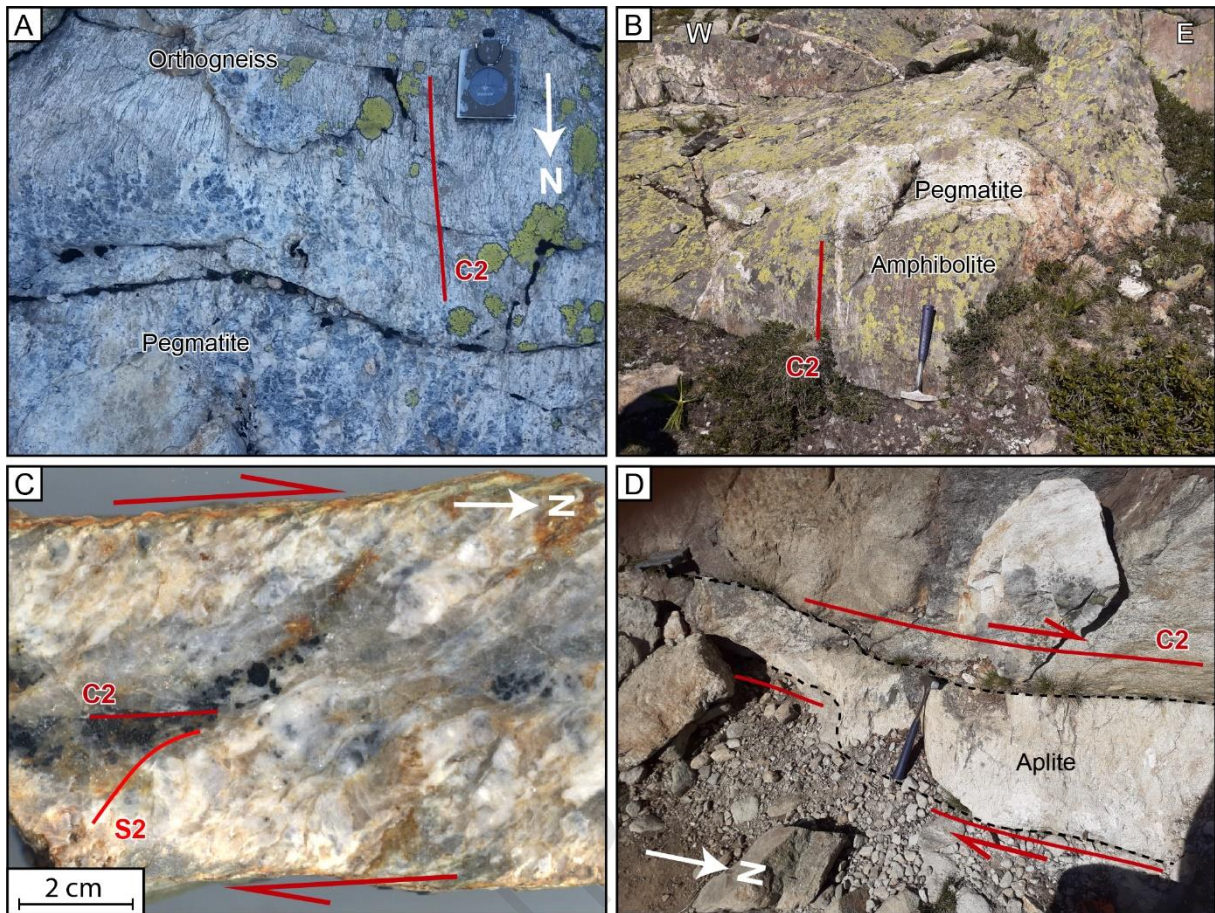
1171 **Fig. 8:** D3 deformation. (A) F3 folds from the western limb of the Servoz syncline, Prarion area
 1172 (N45.894366; E6.750432). (B) Photomicrograph in plane-polarized light showing the
 1173 relationships between S1-S2-S3 planar fabrics in Visean metasedimentary rocks (N45.906481;
 1174 E6.778808). (C) Weakly deformed trondhjemitic melts (highlighted in black) affected by F3
 1175 folds (N45.887808; E6.753523).



1176

1177 **Fig. 9:** Deformation features in the magmatic rocks of the AR and the MB Massifs. Sample
 1178 locations are shown in Fig.1B. (A) Couteray orthogneiss with C2-C'2 shear bands highlighted
 1179 and local preserved leucosomes are visible (orange arrow). (B) L1 mineral lineation indicated

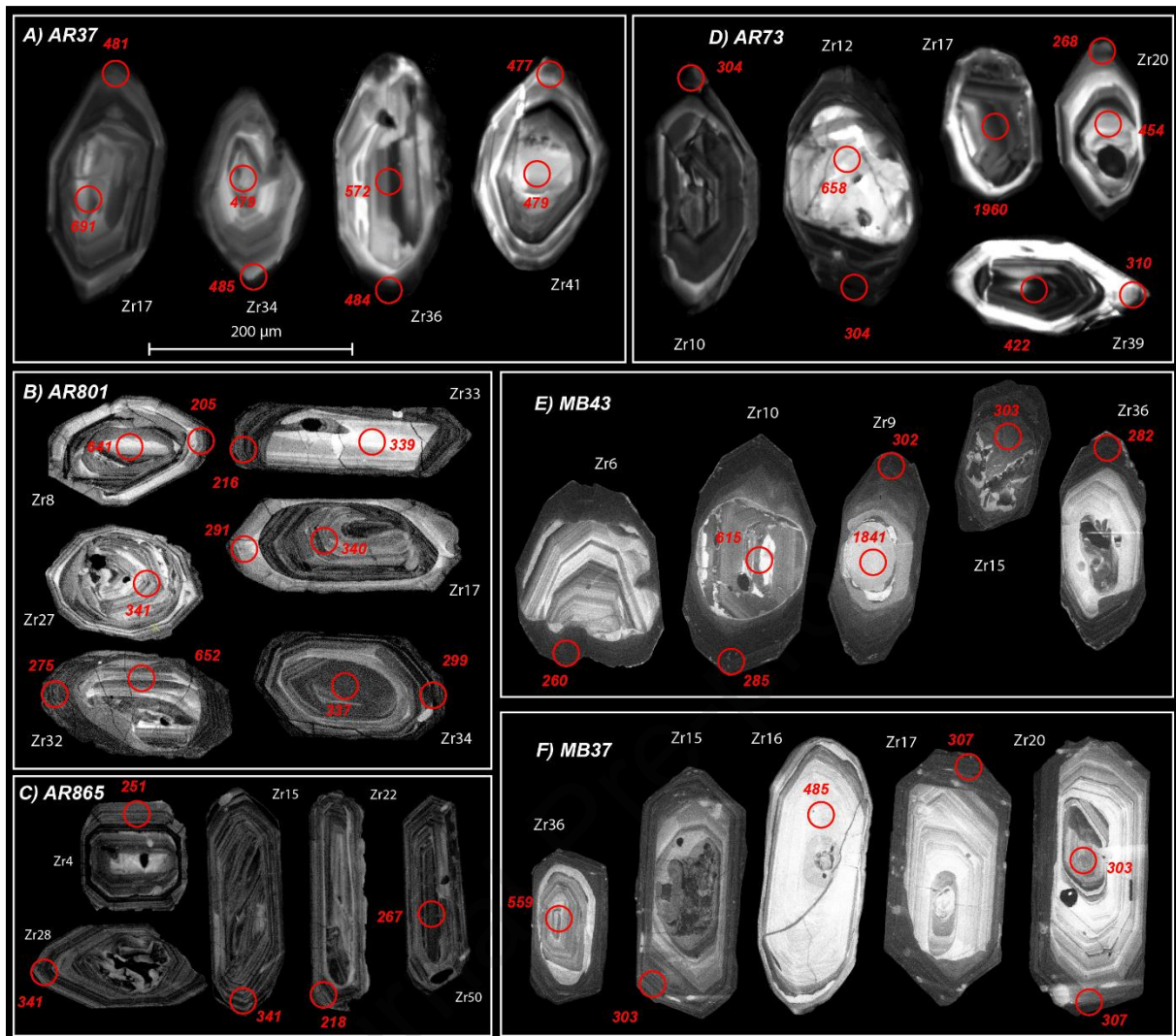
1180 by euhedral K-feldspar from the western part of the Pormenaz granite (AR801). (C) Pormenaz
1181 granite deformed in D2 in the eastern part of the pluton. (D) Photomicrograph in cross-
1182 polarized light of the Montées-Pélessier granite (AR865) with feldspar oriented parallel with
1183 the C2 planes. Orange arrows indicate microfractures in feldspar infilled by quartz
1184 emphasizing the presence of melt during deformation. (E) Vallorcine granite (AR73) cross-
1185 cutting the C'2 planar fabrics of the EBSZ and cross-polarized light microphotograph showing
1186 grain boundary migration recrystallization in quartz aggregates. (F) Montenvers granite
1187 deformed during D2. (G) Photomicrograph in cross-polarized light of the Montenvers granite
1188 (MB43). Orange and yellow arrows indicate microfractures in feldspar infilled by quartz and
1189 polygonal quartz suggesting high temperature deformation. Blue arrows indicate polygonal
1190 quartz deformed at lower temperature. (H) Mont-Blanc granite (MB37) with a magmatic
1191 foliation inferred by the alignment of K-feldspar sub-parallel to C'2. (I) Photomicrograph in
1192 cross-polarized light of the Morcles microgranite (AR1028) without preferred mineral
1193 orientation.



1194

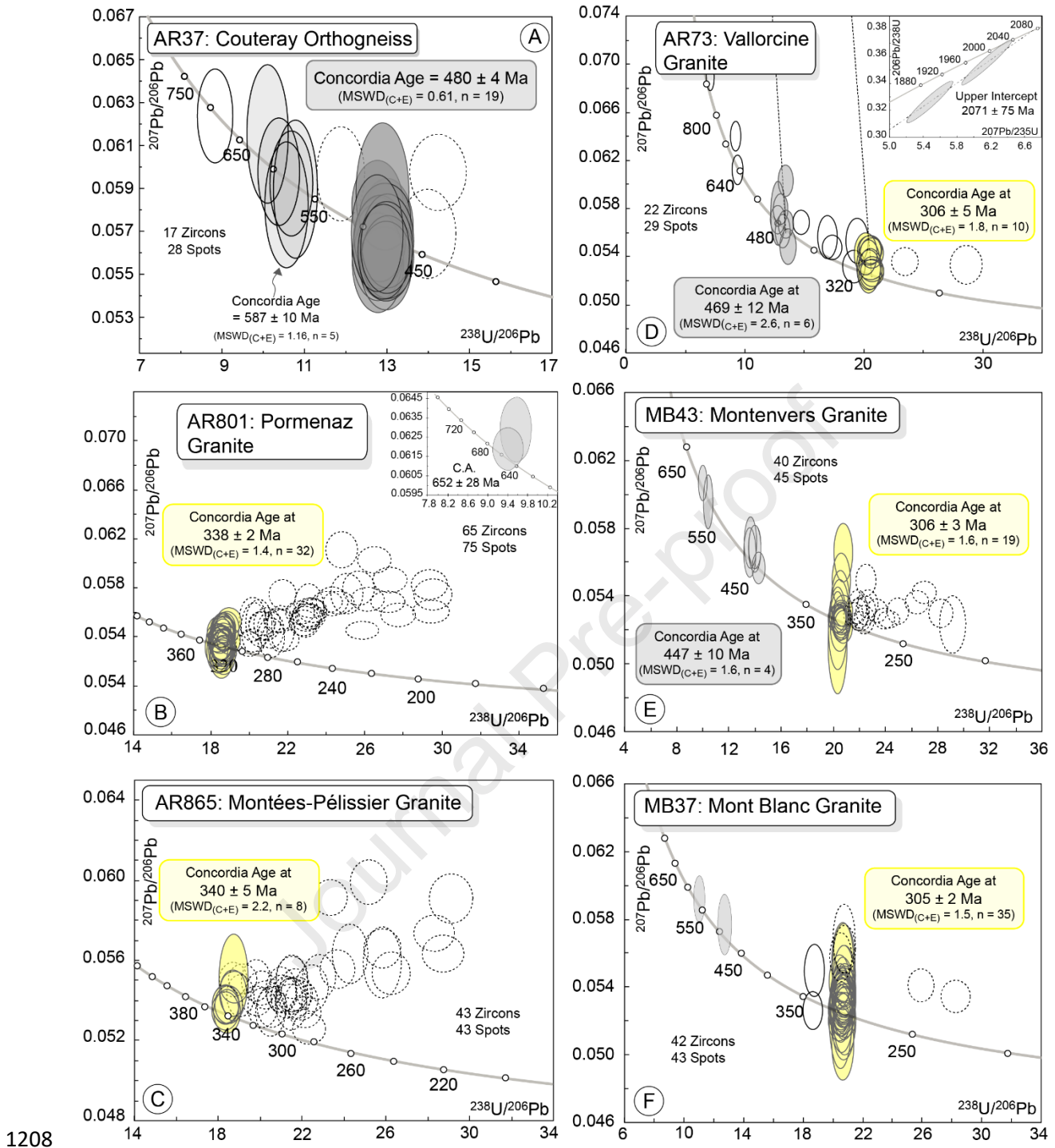
1195 **Fig. 10:** Pegmatitic and aplitic samples. (A) Pegmatite AR833 from the Lac Cornu area
 1196 embedded in a orthogneiss migmatite with diffusive contacts. (B) Pegmatite AR1020
 1197 crosscutting the C2 planes of an amphibolite boudin in the Lac Cornu area. (C) Section of the
 1198 Lacs Noirs pegmatite (AR1006) showing C-S structures. (D) Chéserys aplite (AR916) emplaced
 1199 in a C2 shear zone.

1200



1201

1202 **Fig. 11:** Cathodoluminescence images of zircon grains from: (A) the Couteray orthogneiss; (B)
 1203 the Pormenz granite (sample AR 801); (C) the Montées Pélissier granite (AR865); (D) the
 1204 Vallorcine granite (AR73); (E) the Monteners granite (MB43); (F) the Mont Blanc granite
 1205 (MB37). Red circles indicate the analytical spot locations with the $^{206}\text{Pb}/^{238}\text{U}$ age without
 1206 errors associated. Zr number corresponds to the zircon grain numbers reported in Table S1.
 1207 The bar scale indicated in A is used for all pictures (B to F).



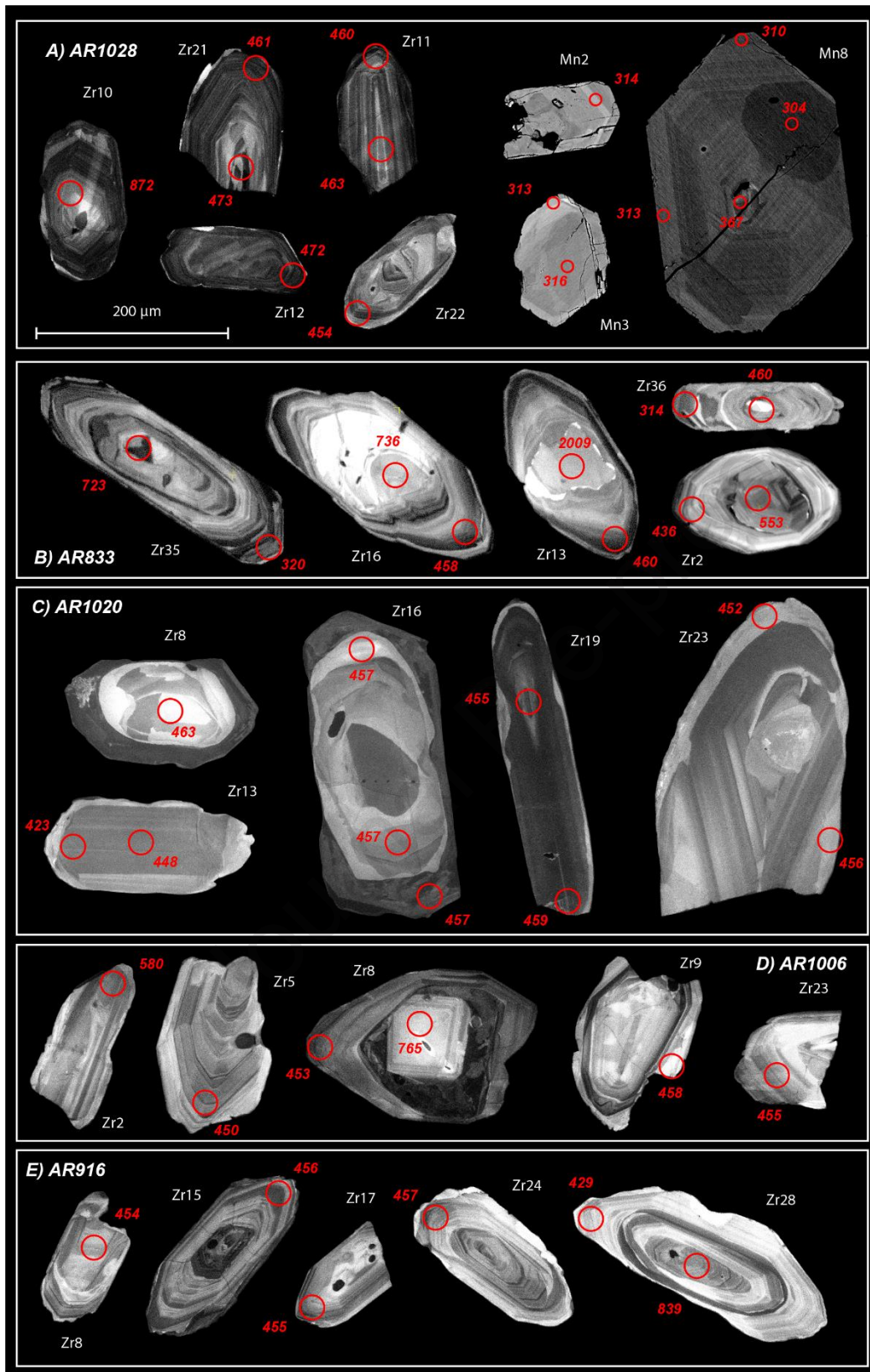
1209 **Fig. 12:** Zircon U-Pb Tera Wasserburg diagrams obtained by LA-ICPMS from (A) the Couteray
 1210 orthogneiss, (B) the Pormenaz granite (AR801), (C) the Montées Pélissier granite (AR865), (D)
 1211 the Vallorcine granite (AR73), (E) the Monteners granite (MB43), (F) the Mont Blanc granite
 1212 (MB37). Error ellipses and uncertainties in ages are $\pm 2\sigma$ level. The discordance of dotted

1213 ellipses is due to radiogenic Pb losses and common Pb contaminations. Dotted and white

1214 ellipses are not considered for the age calculation.

1215

Journal Pre-proof

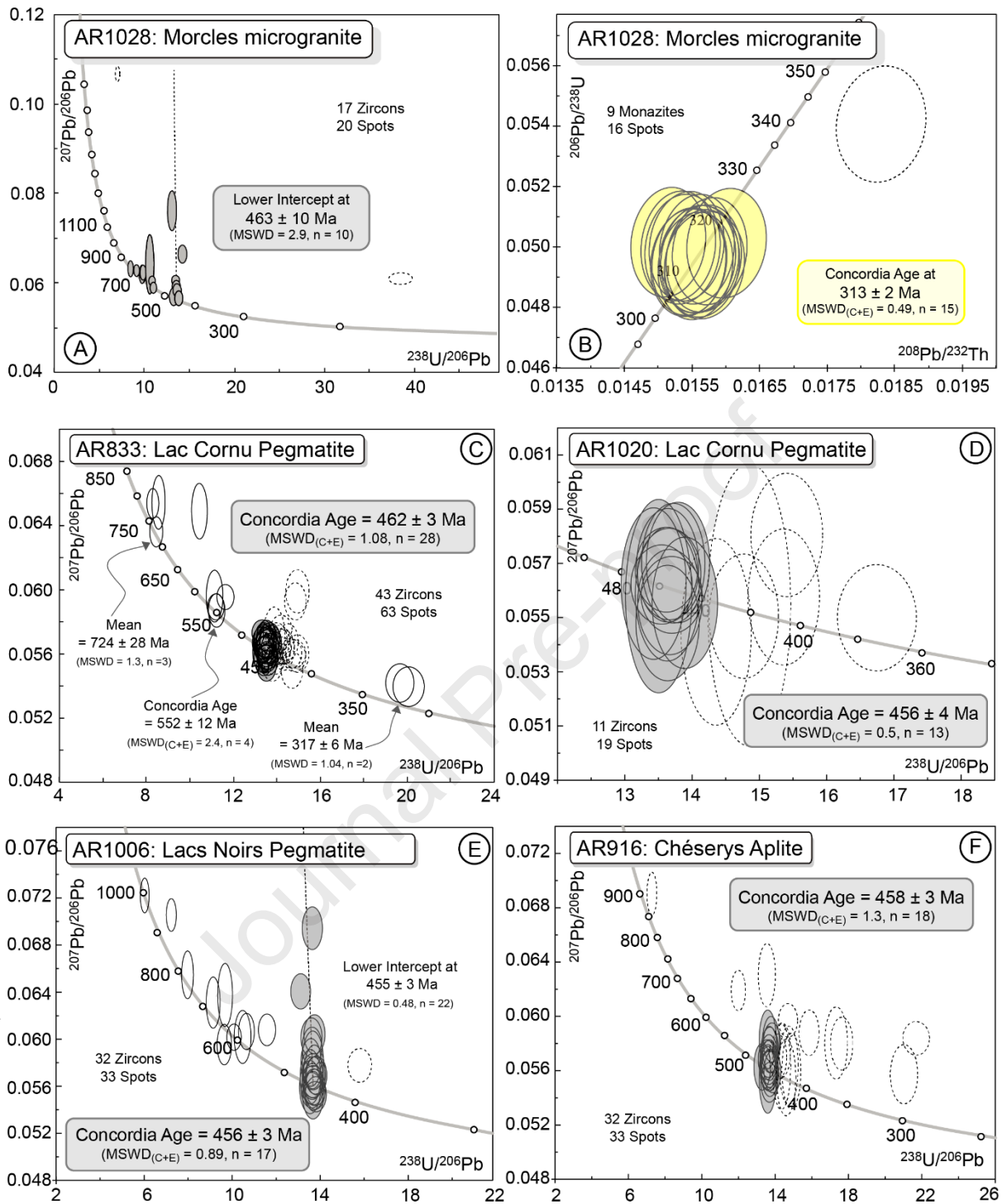


1216

1217 **Fig. 13:** Cathodoluminescence and back-scattered electron images of zircon (Zr) and monazite
 1218 (Mn) grains from: (A) the Morcles microgranite (AR1028); (B) a Lac Cornu pegmatite (AR833);

1219 (C) a Lac Cornu pegmatite (AR1020); (D) the Lacs Noirs pegmatite (AR1006); (E) the Chéserys
1220 aplite (AR916). Red circles indicate the analytical spot locations with the $^{206}\text{Pb}/^{238}\text{U}$ or
1221 $^{208}\text{Pb}/^{232}\text{Th}$ ages measured without the error associated for the zircon and the monazite grains
1222 analysed, respectively. Zr (or Mn) number corresponds to the zircon (or monazite) grain
1223 numbers reported in Table S1. The bar scale indicated in A is used for all pictures (B to E).

Journal Pre-proof



1224

1225 **Fig. 14:** Zircon U-Pb Tera Wasserburg diagrams (A, C, E, F, D) and monazite U-Th-Pb concordia
 1226 diagram (B) obtained by LA-ICPMS: (A and B) on the Morcles microgranite (AR1028), (C and D)
 1227 on the Lac Cornu pegmatites (AR833 and AR1020), (E) on the Lacs Noirs pegmatite (AR1006),
 1228 (F) on the Chéserys aplite (AR916) Error ellipses and uncertainties in ages are $\pm 2\sigma$ level. The

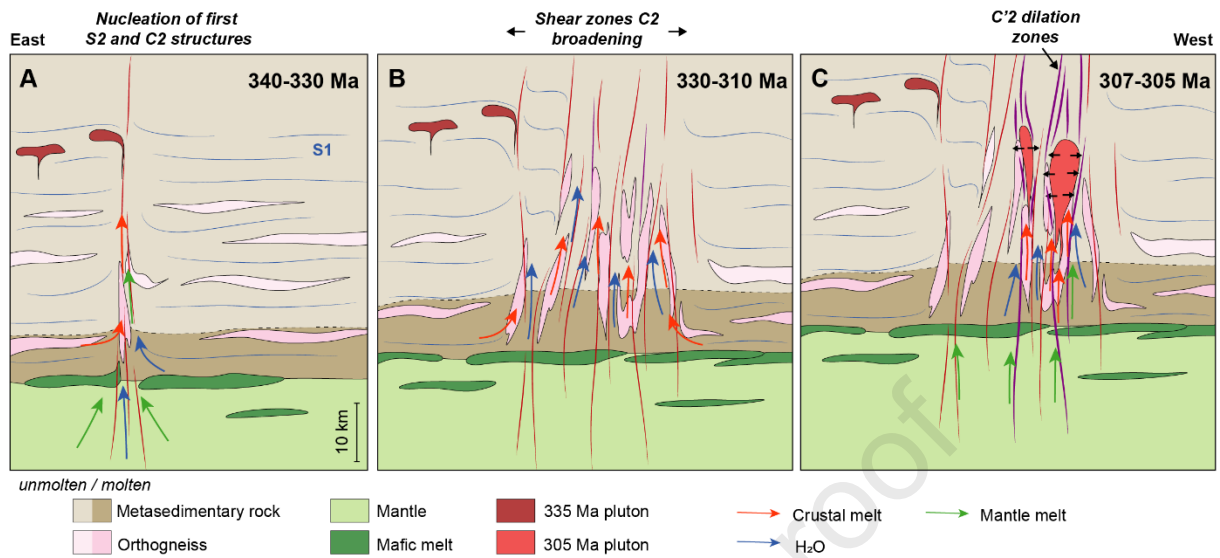
1229 discordance of dotted ellipses is due to radiogenic Pb losses and common Pb contaminations.

1230 Dotted and white ellipses are not considered for the age calculation (see text for detail).

1231

Journal Pre-proof

1232



1233

1234 **Fig. 15:** Tectono-magmatic evolution of the AR and MB massifs. (A) Initiation of the dextral
 1235 shearing after the nappe stacking. The fluids, anatectic lower crustal melts and mantle mafic
 1236 melts are drained upward and form small plutons in the upper crust. (B) Broadening of the
 1237 C2 shear zones drains more fluids that increase the partial melting of meta-igneous rocks
 1238 forming the numerous aplitic and pegmatitic dykes. (C) C'2 shear zones, acting as dilation
 1239 zones, collect anatectic melts and the small mantle supply to form large plutons.

1240

1241 **Table 1:** Sample descriptions and locations

Sample	Rock type	GPS location	Mineral assemblage	Mineral dated	U-Th-Pb age
AR37	Courtenay orthogneiss	N46.019559 E06.907883	Qtz + Kfs + Pl + Ms + Bt	Zircon	587 ± 10 Ma 480 ± 4 Ma
AR801	Pormenaz granite	N45.949951 E06.789104	Qtz + Kfs + Pl + Bt(Chl)	Zircon	338 ± 2 Ma
AR865	Montées-Pélessier granite	N45.917067 E06.77147	Qtz + Kfs + Pl ± Ms ± Bt(Chl)	Zircon	340 ± 5 Ma
AR73	Vallorcine granite	N46.032901 E06.936665	Qtz + Kfs + Pl + Bt	Zircon	306 ± 5 Ma
MB43	Montenvers granite	N45.96768 E06.949665	Qtz + Kfs + Pl + Ms + Bt ± Grt	Zircon	306 ± 3 Ma
MB37	Mont-Blanc granite	N46.063859 E07.08007	Qtz + Kfs + Pl + Bt	Zircon	305 ± 2 Ma
AR1028	Morcles microgranite	N46.193943 E07.043689	Qtz + Kfs + Pl ± Ms ± Bt(Chl)	Zircon Monazite	463 ± 10 Ma 313 ± 2 Ma
AR833	Lac Cornu Pegmatite	N45.956094 E06.853814	Qtz + Kfs + Pl ± Ms	Zircon	462 ± 3 Ma 317 ± 6 Ma
AR1020	Lac Cornu Pegmatite	N45.958210 E06.846594	Qtz + Kfs + Pl	Zircon	456 ± 4 Ma
AR1006	Lac Noirs Pegmatite	N45.966231 E06.871656	Qtz + Kfs + Tur + Ms	Zircon	456 ± 3 Ma
AR916	Chéserys Pegmatite	N45.982963 E06.908710	Qtz + Kfs + Pl + Ms ± Tur ± Grt	Zircon	458 ± 3 Ma

Highlights

- The strain pattern of a portion of the crustal East-Variscan Shear Zone is given.
- The main shear direction is not NE-SW but N-S directed.
- The S-C-C'-like strain pattern controls the transfer and emplacement of magmas.
- Late-orogenic magmas come from H₂O-saturated melting of meta-igneous protoliths.

Author statement

Jonas Vanardois: Conceptualization, Investigation, Writing - Original Draft, Project administration, Funding acquisition

Pierre Trap: Conceptualization, Investigation, Writing - Original Draft, Supervision, Project administration, Funding acquisition

Françoise Roger: Conceptualization, Validation, Investigation, Writing - Review & Editing

Jérémie Melleton: Conceptualization, Writing - Review & Editing

Didier Marquer: Writing - Review & Editing, Supervision, Funding acquisition

Jean-Louis Paquette: Validation, Investigation, Writing - Review & Editing

Philippe Goncalves: Writing - Review & Editing

Florence Cagnard: Investigation, Writing - Review & Editing

Benjamin Le Bayon: Investigation, Writing - Review & Editing

Declaration of interests

The authors declare that they have no known competing financial interests or personal relationships that could have appeared to influence the work reported in this paper.

The authors declare the following financial interests/personal relationships which may be considered as potential competing interests:

Jonas Vanardois reports financial support was provided by Bureau for Geological and Mining Research.

Journal Pre-proof